UiT
THE ARCTIC
UNIVERSITY
OF NORWAY

Faculty of Science and Technology
Department of Geology

Multiproxy reconstruction of past methane emissions at Storfjordrenna Pingos site (South of Svalbard) during the last deglaciation

Anne Paavilainen

Master's thesis in Geosciences, June 2023

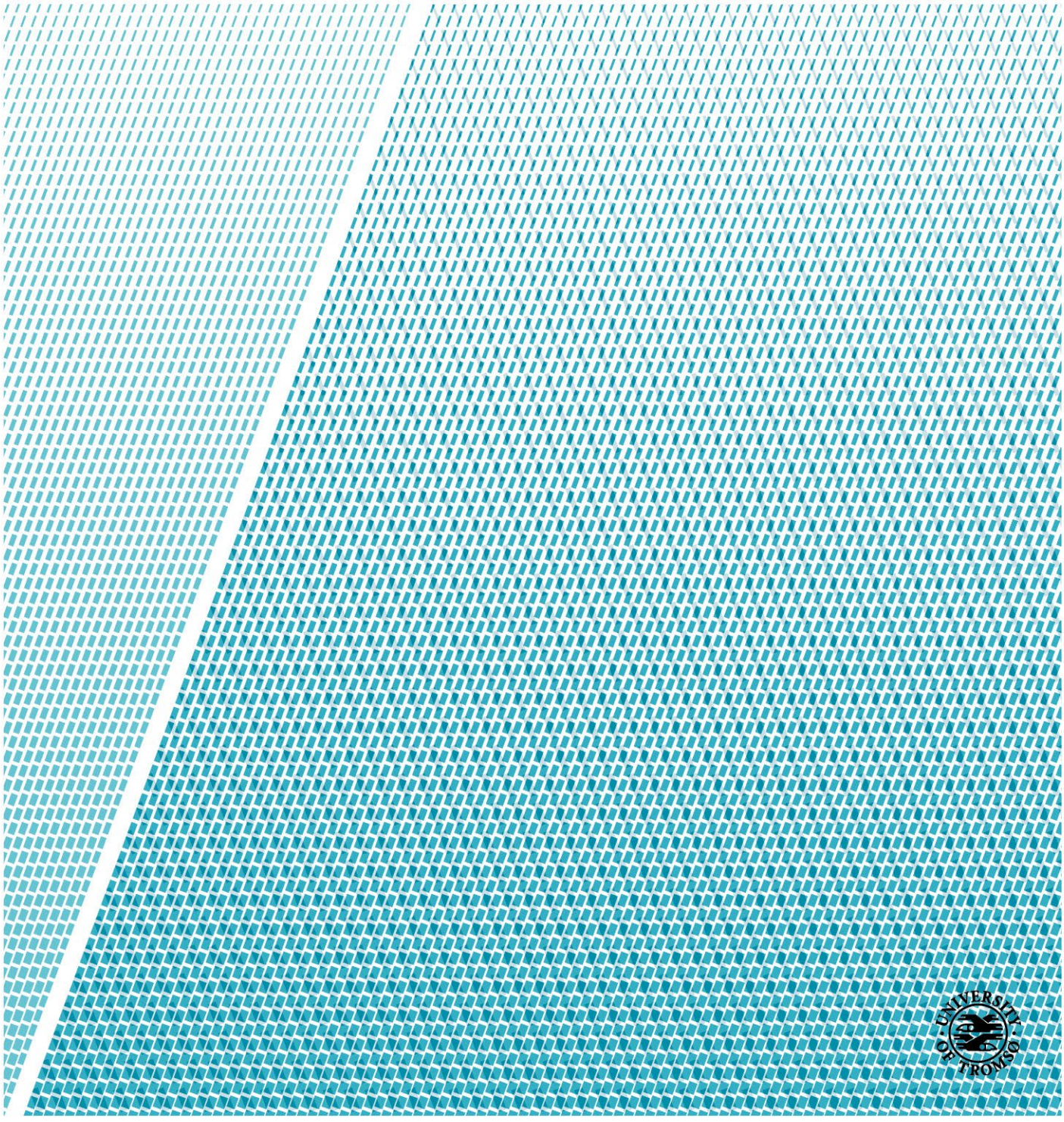

Table of Contents

List of Tables

List of Figures

Foreword

First and foremost, I would like to express my sincere gratitude to my main supervisor Steffen Aagaard Sørensen. Without his dedicated involvement, support, and encouragement during this journey, this master thesis would have not been accomplished. A special thank you for my co-supervisor Katarzyna Melaniuk for all the valuable discussions, advice, and support during this process. I have learned a lot from you. I would also like to thank you my former supervisor Giuliana Panieri and Wei-Li Hong for the opportunity to have some of the data used in this thesis. I would also like to thank the laboratory technicians Trine Dahl, Karina Monsen, Ingvild Hald, and Matteus Lindgren for the assistance. In addition, I would like to thank Christian März for the valuable and interesting discussion and advices.

I would like to express my warmest thanks to Line, -you have always been there for me all this way with ups and downs.

Finally, none of this could have happened without my dear family and friends. I want to express my warmest gratitude for your unconditional support, encouragement, and kindness.

1 Introduction

According to the sixth assessment report (AR6), of Intergovernmental Panel on Climate Change the global surface temperature has risen about 1.1°C since the late 19th century (IPCC, 2023). The Arctic, in particular the Barents Sea is experiencing rapid climate change. It has been observed, that in recent decades due to the progressing climate change the Arctic experiences an expansion of Atlantic water into the Arctic basin, called the "Atlantification" (e.g., Tesi et al., 2021; Spielhagen et al., 2011; Jernas et al., 2010; Årthun et al. 2012; Polyakov et al., 2017). Among others, this process is manifested by severe reductions in sea-ice coverage which results in a large decrease in the thickness of the winter sea ice (Kwok and Rothrock, 2009), and most importantly temperature is increasing four times faster than the global annual average.

Throughout the Quaternary period (2.6 Ma – present) Earth´s climate has been characterized by the oscillations between colder glaciations and warmer interglacial (Hays et al., 1976). These oscillations, with a frequency of ~100 000 years, have been driven by the changes in the Earth`s orbital parameters and the subsequent amount of solar radiation on Earth (Lisiecki and Raymo, 2005; Hayes et al., 1976). The ongoing climate change is rapid and caused largely by anthropogenic greenhouse gas emission into the atmosphere (IPCC, 2023; Howarth et al., 2011). The atmospheric methane concentrations in 2019 were higher than at any point during at least the last 800 000 years (IPCC, 2023).

Methane can be produced within the deep marine sediments by exposing deep complex organic molecules to high temperatures or at the shallow depth by microbial transformation of organic and inorganic carbon (Strąpoć et al., 2020). At temperatures lower than 25°C and pressure between 3–5 MPa, and sediment depth of 300–400 m, methane forms solid, ice-like structures called methane hydrates/gas hydrates (Rupppel and Kessler, 2017). It has been estimated that the gas hydrates constitute the most significant carbon reservoir on Earth (Kvenvolden, 1988). Large amounts of methane are stored within Arctic continental shelves (Judd and Hovland, 2007; Shakhova et al., 2005).

Gas hydrates are sensitive to environmental changes e.g., increasing temperatures or changes in pressure (Maslin et al., 2010). Increasing bottom water temperatures and reduced pressure within the seafloor can result in the destabilization of gas hydrate deposits and in the release of significant amounts of methane from the gas hydrates (Sloan, 1990; El bani Altuna et al., 2021). Abrupt methane emissions from marine sediments may reach the atmosphere, and thus

reinforcing already progressing climate change (Hovland et al., 1993). Given the ongoing ocean warming, there are increasing concerns and a need to assess the gas hydrate stability and the natural emissions of methane from marine sediments in the future (IPCC, 2007).

The main ambition of this thesis was to study the relationship between isotopic signature of fossil foraminifera and past methane emission at Storfjordrenna Pingos site (South of Svalbard) during the last deglaciation in context of past climatic changes. The main objectives were to investigate 1) isotopic signatures ($\delta^{13}C$ and $\delta^{18}O$) of foraminiferal tests from sediments affected by methane, 2) the microstructure and elemental distribution of the foraminiferal tests (SEM-EDS), 3) the solid-state chemical composition of the sediment (XRF), 4) the magnetic susceptibility record of the sediments, 5) the ice rafted debris content of the sediment (IRD), and 6) the subjective foraminiferal abundance record.

2 Theoretical background

2.1 Study site

The study site is located on the north-western part of the Barents Sea (Fig. 1a), on the outer part of the Storfjordrenna Trough. It is located ca. 50 kilometers south from the southern tip of Svalbard archipelago (Fig.1b).

Storfjordrenna is a cross-shelf trough, a seaward extension of the Storfjord. It ends on the continental shelf-break and opens to the Norwegian Sea. The trough is 250 km long and up to 420 m deep and has a width of 125 km on the self-break (Fig. 1b). The trough was formed by a former ice stream and has served since as a drainage route for the eroding ice streams during the glaciations (Laberg & Vorren 1996; Howat et al., 2010).

Numerous cross-shelf oriented channels upon the outer part of the Storfjordrenna trough indicate former ice stream erosion. The study site is in the northernmost channel. Mega-scale glacial lineations (MSGL´s) (Fig. 2c) and several generations of plough marks and grounding zone wedges upon the channels indicate alternating ice- sheet dynamics during the last deglaciation (Shackleton et al., 2020).

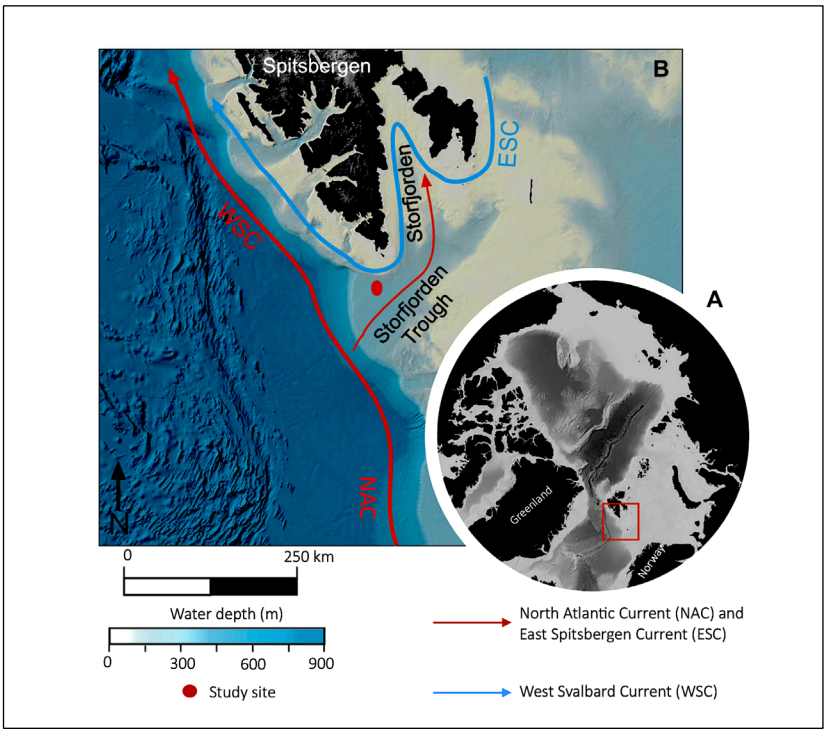

***Figure 1**. **A)** location of the north-western Barents Sea, **B)** The study site at the outer part of the Storfjordrenna Trough. The NAC transports warm Atlantic Water (AW) and the WSC transports cold Arctic Water (ArW) to the study site.*

Five distinct, conical, subcircular and elongated Gas Hydrate Pingoes (GHP; Serov et al., 2017) are found within a 2.5 km^2 area at the study site (76 °N 16 °E). The GHPs stand out 8 – 10 m higher than the surrounding seafloor and they are 280 – 450 m in diameter. The present-day water depth at the study site is ~ 380 m (Fig. 2a, c) The GHPs are consisted of soft cohesive muds, gas hydrates and authigenic carbonates (Serov et al., 2017). They leak dissolved and free methane gas (Hong et al., 2017) (Fig. 2c).

The GHP 5 (Fig. 2b) is considered being in a "post-active stage" based on the lack of 1) hydroacoustic anomalies in the water column above the topographic summit (Serov et al., 2017), 2) seismic indications of free gas in the subsurface (Sen et al., 2018), and 3) gas hydrates in the subsurface sediments (Sen et al., 2018).

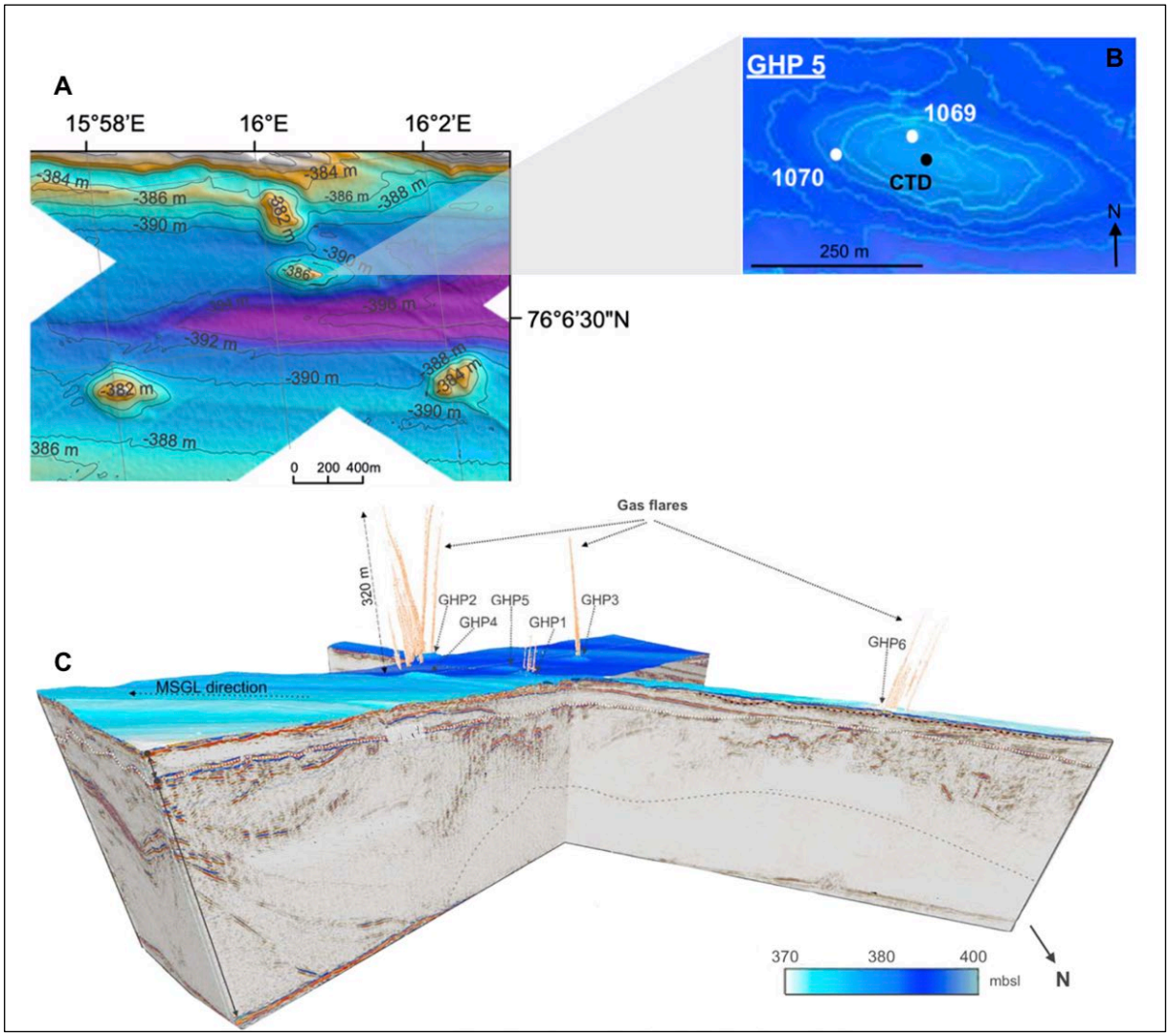

Figure 2. A) *The Pingo site,* ***B****) Close-up for the Gas Hydrate Pingo 5, sampling sites for the CTD and the cores 1070 and 1069,* ***C)*** *The seafloor with methane flares and mega scale lineations (MSGL). Modified from Waage, et al., 2019 and El bani Altuna et al., 2021.*

The internal structure of the shelf

The subsurface shelf structure beneath the GHPs is consisted of the following units (from top to bottom): 1) glacial unit: Pleistocene glacial sediments (thickness: 35–150 m) (Vorren et al., 1991); 2) pre-glacial unit: Paleocene sedimentary rocks (100–500 mbsf) (Waage et al., 2019); 3) Pre-Devonian basement rocks (2–5 km) that are part of the regional Hornsund Fault Zone (HFZ) (Faleide et al., 2008) (Fig. 3).

Below the GHPs, vertical, focused fluid flow structures, gas chimneys extend downwards - through the glacial deposits into the faults and fractures within the underlying tilted and folded Paleocene sedimentary rocks. The faults are linked to an even deeper-seated Pre-Devonian basement rocks (Waage et al., 2019) (Fig. 3).

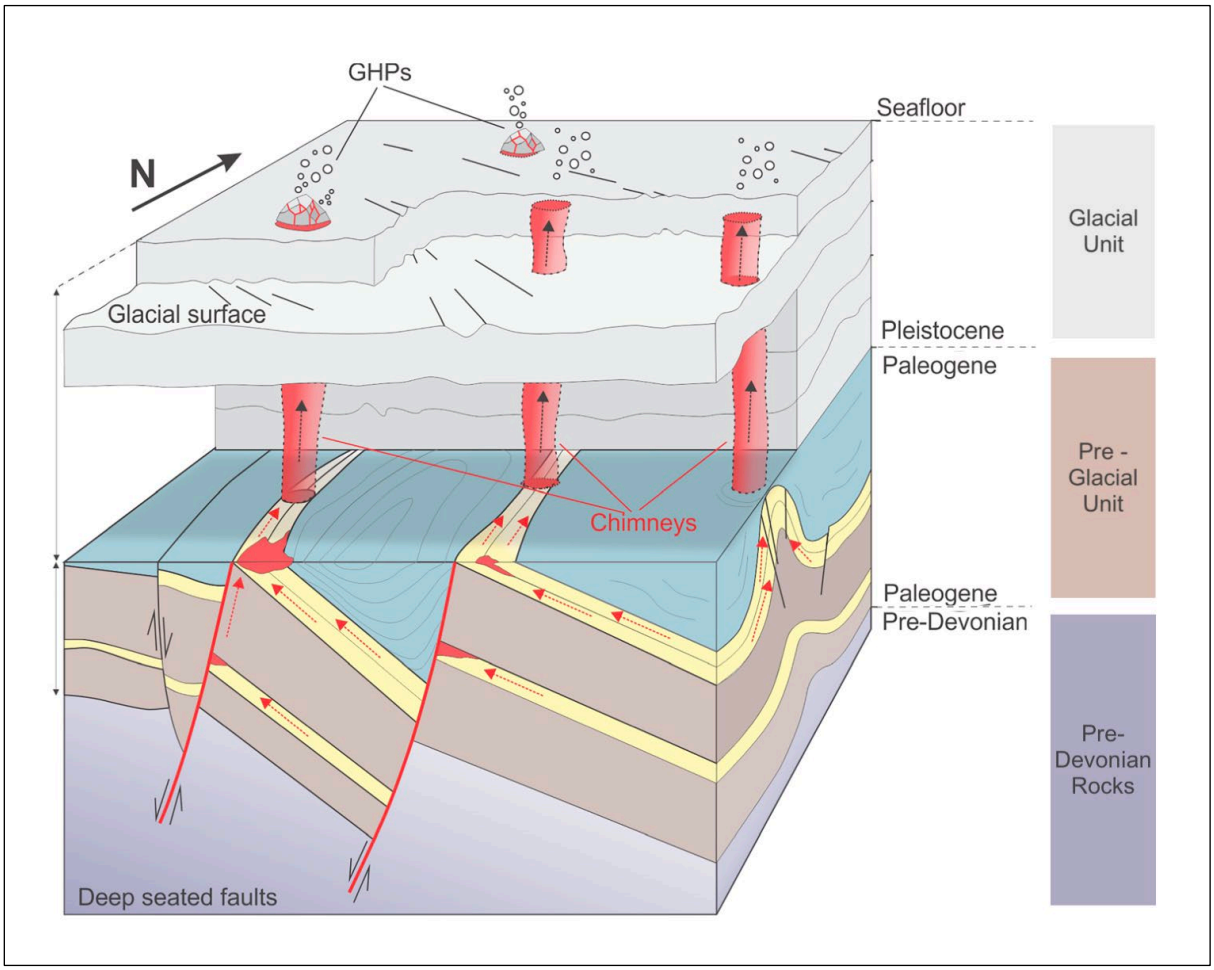

Figure 3. *The internal structure of the shelf comprising the Glacial Unit, Pre-Glacial Unit, Pre-Devonian Rocks and the chimneys connecting them beneath the GHP´s. Modified from Waage et al., 2019.*

2.1.4 Modern oceanography

The oceanography of the outer part of the Storfjord Through is characterized by the interplay of two contrasting main water masses, the warm Atlantic Water (AW) and the cold Arctic Water (ArW) (Loeng, 1991) (Fig. 1b; Table 1).

Table 1. *The water masses at the Storfjordrenna Pingos site.*

	Water mass	Salinity (‰)	Temperature (°C)
Main water masses	Arctic Water (ArW)	34.3 – 34.8	< 0.0
	Atlantic Water (AW)	> 34.95	> 0.0
Locally produced water masses	Brine-enriched Shelf Water (BSW)	> 35.00	< 0.0
	Polar Front Water (PW)	34.8 – 35.0	-0.5 – 2.0

AW is transported into the Storfjordrenna Trough by the eastward flowing branch of the North Atlantic Current (NAC). AW is a warm (>3°C) and highly saline (>35psu) and keeps the western Svalbard climate substantially milder during the wintertime than at comparable latitudes in the other parts of the world. It also keeps the western part of the Svalbard free of sea ice. The main branch of NAC continues northward as a West Svalbard Current (WSC). The AW occupies the entire water column during the summer and autumn (Loeng, 1991).

ArW is cold (< 0.0°C), low-saline (34.3 – 34.8psu) and isotopically lighter surface water mass. ArW is transported into the Storfjordrenna Trough from the Arctic Ocean by the East Spitsbergen Current (ESC). East Spitsbergen Current flows southward along the east coast of Svalbard, and via Storfjord continues as a Sørkapp Current along the outer Storfjordrenna Trough (Loeng, 1991).

The density gradients between the AW and ArW forms the Arctic Front Zone that follows approximately the sea-ice edge and is a highly productive zone. The Arctic Front Zone defines the maximum sea-ice extent during winters (Vinje 1977; Loeng 1991). In addition, locally produced water masses influence the outer part of the Storfjordrenna Through. At the Polar

Front AW and ArW mixes intensely forming local water mass, the Polar Front Water (PFW) with temperature between -0.5 and 2.0°C and salinity of 34.8 – 35psu (Loeng, 1991).

Brine-enriched Shelf Water (BSW) is produced in inner Storfjord during the winters. During the brine season, BSW can outflow from Storfjord into the Storfjordrenna Through as relatively weak bottom water plumes. The BSW is cold (< 0.0°C), saline (> 35psu) water mass (Midttun, 1985; Haarpaintner et al., 2001).

2.1 Late Quaternary climate history of Svalbard

During the Last Glacial Maximum (LGM) around 20 000 years ago, Barents Sea Ice Sheet (BSIS) reached its maximum extent over the whole Svalbard-Barents Sea region (Vorren and Laberg, 1996). In the north-western Svalbard, the Storfjordrenna Ice Stream, a major outlet of the Barents Sea Ice Sheet, reached all the way to the continental shelf break, occupying the whole Strodjorden and Storfjordrenna Trough (Laberg and Vorren 1996; Jessen et al., 2010; Rasmussen and Thomsen, 2021). Studies show that the Storfjordrenna Ice Stream consisted of three distinct sub-ice-streams and the Pingo-site located beneath the northern sub-ice-stream, fed by ice draining from terrestrial Svalbard through Storfjorden (e.g., Pedrosa et al., 2011; Lucchi et al., 2013; Shackleton et al., 2020).

The Last Glacial Maximum was followed by abrupt global rise in temperature, a climatic shift, that led to the rapid retreat of the Barents Sea Ice Sheet from the continental shelf break and deglaciation. Based on several marine records, the beginning of the deglaciation started around 20,500 ± 500 cal. a BP (e.g., Jessen et al., 2010; Jessen and Rasmussen, 2019; Rasmussen and Thomsen, 2021). Various paleoclimatic and -environmental records from the shelf have shown that the deglaciation was climatically warm, but unstable and episodic in nature, caused by the interplay between climate, ocean circulation and the ice sheet activity (e.g., Jessen et al., 2010; Rasmussen and Thomsen, 2014 and 2021; Jessen and Rasmussen, 2019).

The retreat of the Storfjordrenna Ice Stream was interrupted by three colder stadial: 1) Heinrich stadial (HS1) 17 500 – 14 600 cal. years BP, 2) Older Dryas (OD) between the Bølling-Allerød interstadials, 3) Younger Dryas (YD) 12 800 – 11 700 cal. years BP. At the beginning of the Bølling-Allerød interstadial (14 600 – 12 800 cal. years BP) the Storfjordrenna Ice Stream retreated rapidly due to rapid global rise in temperature (Rasmussen et al., 2014a; Rasmussen and Thomsen, 2021). These climatic episodes can be recognized as distinct faunistic and lithological shifts in the sedimentological records in the Storfjorden Trough and in the whole

Barents Sea region (Svendsen et al., 1996; Aagaard-Sørensen et al., 2010; Jessen et al., 2010; Junttila et al., 2010; Nielsen and Rasmussen, 2018).

By the beginning of the Holocene interglacial (11 700 cal. years BP - present), the Storfjordrenna Trough had become ice-free (Rasmussen and Thomsen, 2021). The Holocene climate has been relative stable, but some general climatic trends have been recognized 1) Globally increasing temperatures of ~0.6°C from Early Holocene to Holocene thermal maximum (~11 700 – 9500 ka), 2) the "Holocene thermal maximum/Climatic optimum" (~9.5 – 5.5 ka) (Rasmussen et al., 2014a) and 3) "Long-term cooling" of 0.7°C (~5.5 – 100 years ago) (Lowe and Walker, 2015). Some Early Holocene key climatic events have been recognized 1) Early Holocene climatic cooling event at 11.5 ka (Rasmussen et al., 2007), 2) Early Holocene diatom maximum 10 100 +/- 150 to 9840 +/- 200 cal years BP (Stabell, 1986; Jessen et al., 2010), 3) Early Holocene climatic cooling at 9.3 ka (Rasmussen et al., 2007), 4) Early Holocene climatic cooling around 8.2 ka (Rasmussen et al., 2007, 2014). In addition, some Late Holocene key climatic events have been identified1) Late Holocene 4.2 ka event, 2) Roman Warm Period, 3) Medieval Warm Period, 4) Dark Ages Cold Period, and 5) The little Ice Age (LIA) and the modern anthropogenic warming (Zamelczyk et al., 2020).

2.2 Palaeoceanographic proxies

Proxies are indirect measurements of past environmental and climatic conditions. In palaeoceanographic studies paleoclimates are reconstructed with proxy data because instrumental records do not reach far enough back in time. Marine sediments are undisturbed geological archives that preserve various signal carriers. Signal carriers are divided into biological-, geochemical-, physical- and sedimentological proxies (Bradley, 2015). The proxies used in this thesis are described below.

2.1.1 Biological proxies

Foraminifera are unicellular, marine organisms, known from the Early Cambrian, and they are important in paleoclimate studies and as biostratigraphical indicators (Armstrong & Brasier, 2005). They are very abundant in the modern oceans, and they comprise > 90% of deep-sea biomass and > 55% of the Arctic biomass (Murray, 2006). They have wide geographical distribution from polar to tropical regions. Foraminifera live either among the surface waters (planktonic species) or on/within the seafloor sediments (benthic species). The abundance and distribution of foraminiferal species are controlled by various environmental factors

(Armstrong & Brasier, 2005; Murray, 2006). To protect the cytoplasm from chemical, physical, and biological stress foraminifera secretes a hard shell (tests) made of either calcite ($CaCO_3$), aragonite, silica, or build an agglutinated test from particles presented in the environment. After dying, organic cytoplasts decay and empty foraminifera tests get buried into the marine sediments and become fossilized. The abundance and composition of the fossil foraminiferal assemblages within the marine sediments reflects the paleoenvironmental conditions at the site at the time of their deposition.

Planktic foraminifera live passively floating in the surface waters. Bé (1977) divided planktic foraminifera into three broad groups based on depth of their habitat 1) shallow water species, 2) intermediate species, and 3) deep planktic species. A variety of feeding strategies and morphological adaptations are found to be related to the living depth (Murray, 2006). Planktic foraminifera species show a wide range of behaviors and diet. Depth-correlated factors such as photic conditions, nutrient levels, the amount of dissolved oxygen and temperature are limiting factors in their distribution. Deviations from the optimal conditions lead to gradational reduction in the vital functions, eventually leading to death (Arnold and Parker, 1999). Foraminiferal abundance patterns are believed to reflect primary productivity and they are also intolerant to brackish water (Bé and Tollerlund, 1971).

Benthic foraminifera are the most common Protists within the seafloor sediments at the Barents Sea (Steinsund et al., 1994). Benthic foraminifera live either at the sediment-water interface or within the sediment. Various studies have shown that physical, chemical, and biological parameters may limit the distribution of species. These parameters include e.g. temperature (Rasmussen and Thomsen, 2017), amount of oxygen (Alve and Bernhard, 1995), food supply (Rasmussen and Thomsen, 2017), hydrodynamics of the bottom water (Gustafson and Nordberg, 2001), or pH (Rasmussen and Thomsen 2014b, c). According to vertical microhabitat preferences benthic foraminifera have been divided into three groups 1) epifaunal, individuals that live above the water-sediment interface, 2) shallow infaunal, live within the water-sediment interface, and 3) infaunal, foraminifera that lives within the sediment (Jorissen, 1999 and references therein). As both food supply and sediment water oxygen concentration are influenced by the primary production at the surface waters, which in turn is controlled by the surface water mass type, seasonality and climate, the benthic foraminifera can be used as indirect paleoclimate/environment indicators (e.g., Polyak et al., 2013; Seidenkrantz 2013).

2.1.2 Geochemical proxies

Stable isotopes of oxygen (O) and carbon (C) measured in foraminiferal tests are widely used in the paleooceanographic studies. Both oxygen and carbon have more than one stable isotope which differ from each other by their molecular weight. Physical and chemical fractionating processes like evaporation, condensation, and photosynthesis favor one of the isotopes over the other (Ravelo and Hillaire-Marcel, 2007). This leads to enrichment or depletion of a certain isotope in certain environments (Faure, 1998). Because foraminifera biomineralizes their $CaCO_3$ tests by secreting the carbon and oxygen from the ambient sea- or porewater the isotopic composition of the isotopic signature of ambient seawater is recorded and preserved in foraminiferal tests. The isotopic composition of fossil foraminiferal calcite can be measured and the isotopic signal can be used to reconstruct the paleoenvironments in which foraminifera secreted their tests. (Armstrong & Brasier, 2005; Pearson, 2012). Foraminifera are found to secrete their $CaCO_3$ tests close to the isotopic equilibrium with the sea- and porewater (McCorkle et al, 1990). However, small, but noteworthy disequilibrium effects do exist caused by biological and ecological fractionation. These factors must be considered when interpretating the isotopic signatures (Armstrong & Brasier, 2005; Ravelo and Hillaire-Mercel, 2007).

As the heavier isotopes of oxygen and carbon are rare, their low abundances in the sample can be quantified accurately as ratios to the more common lighter isotopes in the sample ($^{18}O/^{16}O$ and $^{13}C/^{12}C$). The isotopic ratio is expressed as `delta` notation (δ) and as departures in parts per thousand (‰) from a laboratory standard (Vienna Pee Dee Belemnite, VPDB) (Armstrong & Brasier, 2005; Ravelo and Hillaire-Mercel, 2007).

Oxygen stable isotope

The oxygen isotopic composition ($^{18}O/^{16}O$) of the seawater is regulated by the fractionating processes evaporation and precipitation. The lighter $H_2{}^{16}O$ evaporates easier from the ocean to the atmosphere than the heavier $H_2{}^{18}O$. In contrast, the heavier $H_2{}^{18}O$ precipitates easier from the atmosphere to the ocean than the lighter $H_2{}^{16}O$, this fractionating process is called Raleigh Distillation (Armstrong and Brasier, 2005). During the periods of cold climate the removal of the heavier $H_2{}^{18}O$ from the atmosphere is enhanced because cold air holds less vapor. The atmosphere, and subsequently the ice caps via precipitation, get enriched in the lighter $H_2{}^{16}O$. The increase of the heavier $H_2{}^{18}O$ in the sea water is called the Ice Volume Effect (Armstrong and Brasier, 2005). The changes in the seawater $\delta^{18}O$ and subsequently in the isotopic

composition in foraminiferal $CaCO_3$, reflect the variations in total ice volume on Earth. Sediment cores from all over the world have revealed the same general consistent primary foraminiferal $\delta^{18}O$ signal reflecting the cyclic variations in the Quaternary climate. Five Marine Isotopes Stages (MIS 1-5) have been defined from the isotopic record comprising the last ~130 000 years. In the $\delta^{18}O$ curve, high $\delta^{18}O$ values correspond to the glacial stages and are numbered with even numbers (MIS 2 etc.). Low $\delta^{18}O$ values correspond to the interglacial stages and are numbered with uneven numbers (MIS 1 etc.). MIS stages can further be divided into substages, stadials and interstadials and are given letter denotation (e.g., 5a-d). Terminations, rapid transitions between the glacials and interglacials, are given roman numerals (Termination I, etc.). Marine Isotopes Stages enable stratigraphical correlation between cores (Bradley, 2015). The global ice volume signal of planktonic foraminifera can be altered by the local sea surface temperature and salinity changes (Ravelo and Hillaire-Mercel, 2007). These local imprints can be avoided by measuring the isotopic signal from the benthic foraminifera as they secrete their calcite tests in the relatively stable bottom water/pore water conditions (Pearson, 2012).

Carbon stable isotope

The $\delta^{13}C$ of a foraminiferal test reflects the carbon isotopic composition of the Dissolved Inorganic Carbon ($\delta^{13}C_{DIC}$) species in the seawater such as carbon dioxide CO_2, and the bicarbonate ions HCO^-_3 (Mackensen et al. 2006; Wollenburg et al. 2015) the global level, the $\delta^{13}C_{DIC}$ of the mean ocean is primarily influenced by the changes in the size of the terrestrial biosphere as the photosynthesis favor the lighter ^{12}C isotope over the heavier ^{13}C isotope leaving the atmosphere and the ocean enriched in ^{13}C. In addition, the $\delta^{13}C$ of the seawater can be influenced by the local changes in the water masses and the balance between the photosynthesis and respiration (Ravelo and Hillaire-Mercel, 2007). The $\delta^{13}C$ measured in foraminiferal calcite is not in isotopic equilibrium with the $\delta^{13}C_{DIC}$ in seawater due to abiotic kinetic isotopic fractionating (Romanek et al., 1992), biological vital effects of the internal foraminiferal carbon pool (Zeebe et al., 1999) and microhabitat effect. These offsets have species-specific differences (McCorkle et al., 1990).

2.1.3 Physical proxies

Magnetic susceptibility is a physical parameter describing the degree to which the sediment can be magnetized in response to an applied external magnetic field. The ability of the sediment to

get magnetized depends on the sediment composition, such as grain size and mineral content (Stoner et. al., 1996). Magnetic susceptibility signal provides useful record for paleoclimate reconstructions, as the grain size and the mineral content of the sediment are resulted from climate-controlled transport mechanisms and depositional processes. Furthermore, it can be used as chronostratigraphic and correlation tool Jessen et al. (2010) created a stacked and dated magnetic susceptibility record for the western Svalbard margin. However, if the primary signal has been affected by early diagenetic processes within the sediment, it cannot be used as reliable stratigraphical tool any longer, but as a record of past diagenetic processes instead (März et al., 2008; Sztybor and Rasmussen, 2017).

2.1.4 Sedimentological proxies

Sea ice houses and transport debris, so called Ice Rafted Debris (IRD). As the ice melts, the debris is released and deposited on the ocean floor. The IRD distribution within the seafloor sediments provides a signal of past ice sheet dynamics at the site (Bennett and Glasser, 2009). The facies architecture of the IRD-rich layers (the abundancy, size, weight, mineral content, and the angularity of the clasts) provide further information about the source of IRD, debris transport mechanisms, distribution, and number of icebergs, melt rate of the sea ice and depositional processes within the water body (Piper and Brisco, 1975; Bennett and Glasser, 2009).

2.1.5 Radiocarbon ^{14}C Dating

Radiocarbon dating (AMS ^{14}C dating) provides reliable estimates of sample/sediment ages and thus reveals the chronological order of climatic events and the rate of past environmental changes. The ^{14}C dating is based on measuring the amount of radioactive ^{14}C isotope from fossilized marine organisms. While living, these organisms absorb radioactive ^{14}C isotope from dissolved CO_2 from the seawater throughout their lives. After dying, the organisms get buried and they stop incorporating new ^{14}C into their tissues. The radioactive C^{14} content of the organism starts to decline back to its daughter isotope N^{14} by beta decay with invariant half-life (T1/2) of 5568 years (Bradley 2015). The ^{14}C content of an organism is a function of time and the radiocarbon dating is based on counting the proportion of the radioactive ^{14}C atoms in the sample, relative to the stable ^{12}C and ^{13}C atoms. The counting is done by Accelerator Mass Spectroscopy (AMS) (Bradley, 2015). Radiocarbon ages are calculated with the ^{14}C "Libby half-life" of 5568 ± 30 years (Stuiver & Polach, 1977). The resulting radiocarbon ages do not equate with the calendar years, due to the atmospheric variations in the ^{14}C concentration (e.g.,

Reimer et al., 2013) thus the conventional radiocarbon ages must be calibrated. The most up to date calibration curve is Marine20 (Reimer et al., 2020) Calibrated ^{14}C dates are expressed as "cal years AD" (Anno Domino) or "cal years BC (Before Christ) (Bradley 2015).

2.3 Methane in marine environments

Methane (CH_4) is a greenhouse gas, ~ 25 times more potent than CO_2, and therefore a significant increase of methane in the atmosphere could contribute to further global warming (Howarth et al., 2011, Ruppel and Kessler, 2017; IPCC, 2007). Methane is produced in anoxic marine sediments from organic and inorganic carbon either as a metabolic byproduct by fermentative archaebacteria (bacterial methane), or by thermogenic degradation (thermogenic methane) (Whiticar, 1999). Large amounts of methane are stored in the form of gas hydrate, dissolved gas, and free gas within the marine sediments in the continental margins worldwide (Kvenvolden 1988).

Under pressure greater than 3 – 5 MPa and temperature lower than 25°C at the so-called **gas hydrate stability** zone, methane forms gas (methane) hydrates (Fig. 4) (Ruppel and Kessler, 2017; Sloan, 1990). Gas hydrates are ice-like crystalline solids, composed of water molecules and gas molecules bonded together by van der Waals forces (Sloan, 1990). The host water molecules form molecular cage-lattices with trapped gas molecules inside. (Sloan, 1990; Kvenvolden, 1993).

The production of gas hydrates is limited to geographic regions, where the flux of organic carbon is high e.g., in continental margins worldwide, where the primary productivity is high, and the organic detritus is transported from the continents to the sea (Paull & Dillon, 2001). The presence of gas hydrates can influence the seafloor morphology by creating craters (Long et al., 1998), pockmarks i.e., shallow seabed depressions (Portnov et al., 2016), gas domes or submarine landslides (Hovland and Svensen, 2006; Koch et al., 2015, Serov et al., 2017; Waage et al., 2019).

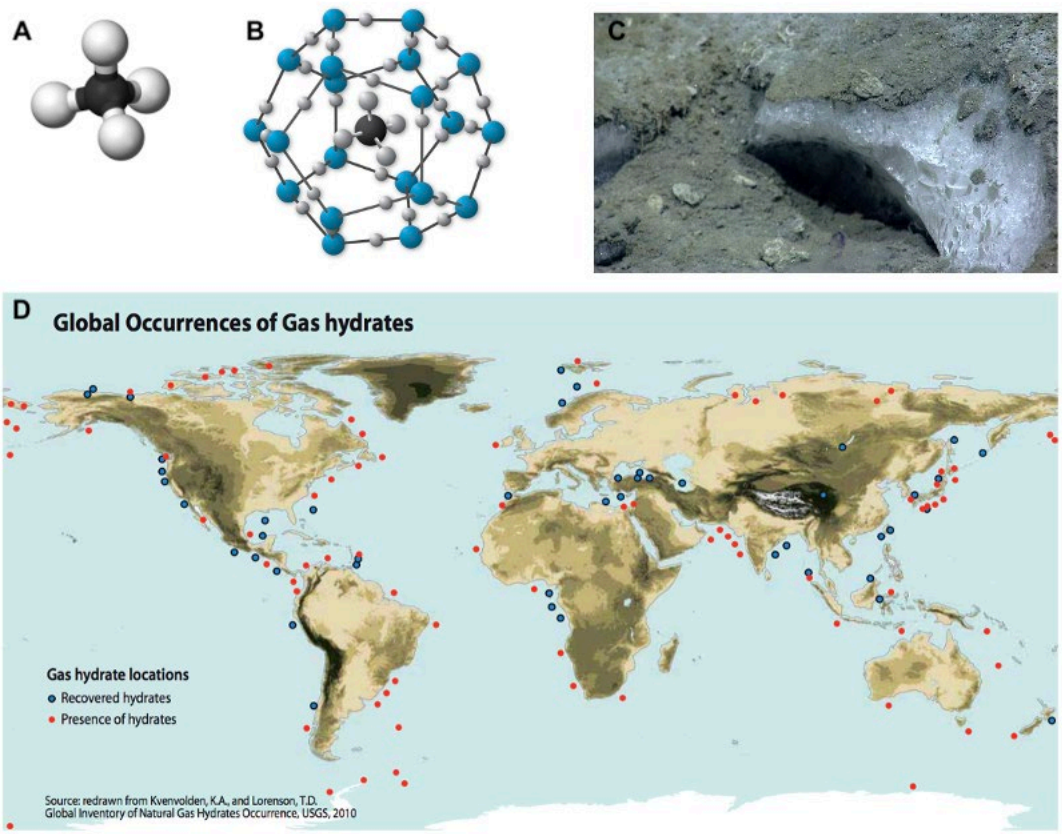

Figure 4. A) *CH_4 molecule, B) Gas hydrate cage,* ***C)*** *Gas hydrates within the sediment,* ***D)*** *map of global distribution of gas hydrates. Map from https://e360.yale.edu/features/the-world-eyes-yet-another-unconventional-source-of-fossil-fuels-methane-hydrates. Methane and methane hydrate: https://oceanexplorer.noaa.gov/facts/hydrates.html Gas hydrates: https://eos.org/editors-vox/could-subsea-methane-hydrates-be-a-warming-tipping-point*

Gas hydrate dissociation can result in the release of significant amounts of methane from the gas hydrates (IPCC, 2007; Phrampus and Hornbach, 2012). Within the marine sediments a large portion of methane becomes consumed in the process of Anaerobic Oxidation of Methane (AOM) mediated by microbial consortiums of Anaerobic Methanotrophic Archaea (ANME) groups and Sulphate Reducing Bacteria (SRB) (Boetius et al., 2000; Orphan et al., 2001). During AOM, sulphate and methane react producing bicarbonate ion (HCO_3^-), bisulphide (HS^-) and water (H_2O) (Boetius et al., 2000) (Eq. 1). The bicarbonates within the sulphate-methane transition zone (SMTZ) might further create carbonate crust (Boetius et al., 2000).

Eq.1: $CH_4 + SO_4^{2-} \rightarrow HCO_3^- + HS^- + H_2O$

The SMTZ is an interface within the sediment column, where upward migrating methane and downward diffusing sulphate (SO_4^2) meet. The depth of the SMTZ depends on several factors such as the transport velocity of methane and sulphate, and thus the vertical location of the SMTZ can vary over time (Boetius et al., 2000; Knittel et al., 2005).

Methane which passes AOM eventually reaches the water column where it is oxidized in a process of aerobic oxidation of methane (MOx; Eq.2) (Knittel et al., 2005).

Eq.2: $CH_4 + 2O_2 \rightarrow CO_2 + 2H_2O$

Methane that passes MOx may potentially reach the atmosphere and contribute to climate change (Shakhova et al., 2014).

The $\delta^{13}C$ signature of methane depends on the origin of the methane. Microbial methane has lighter ^{13}C signatures between -110‰ to -60‰, and thermogenic methane from -50‰ to -20‰. (Whiticar, 1999) As a product of microbial activity (MOx and AOM), the light ^{13}C is released to the ambient water/sediment, as a carbon dioxide gas (CO_2) or bicarbonate ions (HCO_3^{2-}) and this results in changes in the isotopic signature of the ambient seawater and pore water (Whiticar, 1999; Treude et al., 2007) and later in $\delta^{13}C$ of foraminiferal test (Melaniuk et al., 2022).

Marine sediments are a mixture of various solid-state chemical components bounded together into minerals. These minerals are transported and deposited to the ocean floor sediments from various sources from land and ocean. Due to Anaerobic Oxidation of Methane (AOM) within the SMTZ, these minerals can get dissolved by subsequent biogeochemical process within the sediments and new methane derived authigenic minerals precipitated leaving imprint in the solid phase composition. It is possible to infer the past locations of the SMTZ, by tracing relative downcore elemental variations with the X-Ray Fluorescence analysis (XRF). (Funk et al. 2004; März et al., 2008, 2018)

3 Material and methods

3.2 Sampling

3.2.1 Sediment sampling

Two gravity cores with marine sediment were collected from GHP 5 during the CAGE 16 - 5 cruise in June 2016, on board of R/V *Helmer Hanssen*. The core CAGE 16-5 1070 GC (hereafter 1070) was collected from the flank of the pingo and the core CAGE 16-5 1069 GC (hereafter 1069) from top of the pingo (Fig. 2b, Table 2). On board, the gravity cores were cleaned, labelled, and cut into 1-m long sections which were subsequently stored in a temperature-controlled room at +4°C.

Table 2. *Sediment sampling: location, date, ship station, water depth and recovery.*

GHP	Latitude (°)	Longitude (°)	Date	Ship station	Water depth (m)	Recovery (cm)
GHP 5	76°06′42.2″ N	16°00′09.7″ E	26.6.16	1070	385	326
GHP 5	76°06′43.1″ N	16°00′20.0″ E	26.6.16	1069	383	227

Figure 5. *Gravity corer is used for coring soft sediments from the sub seabed. It weights two tons and consists of a six meters long steel core barrel with heavy lead weights (1600kg) on top. The steel core barrel houses an internal plastic core with inner diameter of 10 cm. The vessel is equipped with a winch and a long wire rope to lower the corer above the seafloor. Once allowed to freefall, the gravity corer relies on its weight and the gravitation to penetrate the seafloor. (Photo: https://www.usgs.gov/media/images/gravity-corer-recovers-uppermost-1-2-meters-sediment*

3.2.2 CTD (*conductivity, temperature, and depth)*

During the same cruise the CTD (*conductivity, temperature, and depth*) was measured above the GHP 5, at the station CAGE_16-5_HH_1046 (Table. 3). The CTD measures the physical properties of the water column and consequently enables to identify the present-day water masses at the site.

Table 3. *The CTD station.*

Station	Latitude	Longitude	Date	Depth (m)
CAGE_16-5_HH_1046 CTD	76°6′39.6″ N	16°0′25.812″ E	24.6.2016	380

Conductivity determines the ability of the seawater to transmit an electrical current directly proportional to the total ion content of the water at given temperature. Electrical conductivity of the seawater is measured with a salinometer, an electrical probe inserted into the seawater. The salinometer, electronic thermometer and the pressure sensor are attached to the rigid, circular frame, known as the rosette cluster. The array is lowered and raised through the water column and measurements are made continuously. The CTD instrument transmits the measured signals electronically to the ship, where they are stored and analyzed via a shipboard computer. Conductivity measurements are then calibrated to determinate the salinity of the seawater. Salinity is expressed as ‰ or Practical Salinity Unit (PSU). The temperature measurements are expressed as Celsius degrees (ºC).

3.3 Core processing

3.3.1 X-ray imaging

X-ray imaging was done with GEOTEK MSCL-XCT X-ray imaging system by Dr Wei-Li Hong at the IG, UiT in 2016. Each of sediment cores were placed on a belt and moved through the lead box. The upper part of the lead box contained the X-ray source (160 kV, 19 mA), that passes through the sediment. The resulting signal was amplified and recorded by camera. The signal was then transferred to the computer, where the Geotek acquisition software recorded the basic information about the core.

Later, the Geotek processing software was used to display downcore X-ray intensity logs (gray scale values) including the mean, median, minimum, and maximum values, and the standard

deviations. The purpose was to enhance sequence boundaries and highlight internal sedimentary structures.

3.3.2 Magnetic susceptibility (MS)

Magnetic susceptibility was measured by Dr Wei-Li Hong at IG, UiT in 2016. Magnetic susceptibility was measured with Bartington point sensor integrated on the GEOTEK Multi Sensor Core Logger (MSCL-Slow). Intensity magnetic field of 0.565 kHz was used. Measurement was performed on opened cores. Each of sediment core sections were placed on a belt and moved through the loop in a continuous process with 1-cm measurement interval.

3.3.3 The X-Ray Fluorescence analysis (XRF)

The analysis of the solid phase elemental composition of the sediment was done at the IG, UiT by Dr Wei-Li Hong. The analysis was done with the Avaatech XRF core scanner. Pre-defined measuring time was set to 10 seconds. Based on the atomic number of the element, voltage of 10, 30 or 50 kV was used. The current was 1000 μA. No filter was used. The measurements were carried out with 10 mm interval and reported as counts per second (cps).

According to the commonly used procedure, the core halves are taken out of the cooling room one day before the XRF-measurements to allow the sediment to reach the room temperature. On the measuring day, the surface of the sediment is smoothed with a plastic card perpendicular to the long core axis to avoid cross-contamination. Afterwards the surface of the sediment is covered with 4 μm thick film to avoid contaminations during the measurements (Forwick, 2013).

In total, 27 elements were measured by the XRF scanner (see appendix), but S, Ba, P, Mn, and Fe were chosen for closer study as indicative elements of diagenetic processes. The compositional data was expressed in terms of logarithms of ratios (log-ratios) of two elements to minimize closed sum and matrix effects (Weltje and Tjallingii, 2008). The elements were normalized against Rubidium (Rb) since it is easy to measure and conservative element.

3.3.4 Sampling, Freeze drying and wet sieving

Sampling and freeze drying were done by Dr Haoyi Yao at IG, UiT. The working halves were subsampled into 1-cm thick slices. The sampling interval was 10 cm. To avoid contamination, the sampling spatula was cleaned between every sample. Sediment samples were transferred to

plastic bags and kept in freezer (-20°C) overnight. On the following day, the samples were freeze dried to remove the water content from the sediment. The freeze drying was done using Christ Alpha 144 freeze dryer.

The sediment samples were wet washed through sieves with a mesh size of 250, 100, and 63µm. To avoid contamination, sieves were cleaned (running water, sonic bath, and compressed air) between every sample. Residues were collected on a filter paper and kept at +40 overnight. Dried residues were weighed and kept in labelled pre-weighted plastic bags.

3.3.5 Stable isotope analysis

For the stable isotope analysis ($\delta^{13}C$ and $\delta^{18}O$) empty tests of planktic and benthic foraminifera were hand- picked with a sharp brush using stereomicroscope Leica CLS 150X - MZ12.5. Undamaged foraminiferal tests were picked from designated intervals (every10-cm) with fraction seize 100 - 250µm and stored in Labco Exetainer vials. Approximate 10 planktic and benthic specimens were picked from each sample. The selected planktic species was the common polar species *Neogloboquadrina pachyderma* (sinistral) (Ehrenberg, 1861). For benthic species the most numerous among the core species; *Cassidulina neoteretis* (Seidenkrantz, 1995) (core 1070) and *Cassidulina reniforme* (Nørvang, 1945) (core 1069) (Table. 4) were picked.

Table 4. *Stable isotope analysis: foraminifera species, cores, size fraction, picking intervals and number of picked specimens.*

Core	Species	Reference	Size fraction	Picking interval (cm)	Picked specimens (No.)
1070	*N. pachyderma*	Ehrenberg, 1861	100 - 250µm	10	~ 10
1070	*C. neoteretis*	Seidenkrantz, 1995	100 - 250µm	10	~ 10
1069	*N. pachyderma*	Ehrenberg, 1861	100 - 250µm	10	~ 10
1069	*C.reniforme*	Nørvang, 1945	100 - 250µm	10	~ 10

The stereomicroscope Leica CLS 150X - MZ12.5 with the maximum magnification of 1000X was used. To avoid contamination, the tools used for picking were cleaned between every sample with compressed air. The identification of the species was based on morphological features according to Loeblich and Tappan, 1988.

Before the analyses foraminiferal tests were cleaned with methanol to remove possible sediment remnants. Measurements were done with the Elemental Analyser – Isotope Ratio Mass Spectrometer (EA-IRMS), using a Thermo-Fisher MAT253 IRMS with Gasbench II Mass Spectrometer at the IG UiT. Results were given in standard delta (δ) notation (in parts per thousand ‰) relative to Vienna Pee Dee Belemnite (VPDB). The $\delta^{18}O$ values from the core 1070 were corrected for ice volumes according to Fairbanks 1989. Reported precision was estimated to be ± 0.07 ‰ for $\delta^{13}C$ and ± 0.15 ‰ for $\delta^{18}O$ by measuring the certified standard NBS-19.

3.2 Radiocarbon dating (AMS – ^{14}C)

To establish the age of the oldest interval (core 1070, depth 116 – 117 cm), AMS – ^{14}C dating was performed on fragments of shells of unidentified bivalve species (Table 5).

Table 5. *Radiocarbon dating: core and depth, dated material, ^{14}C age and calibrated age in years before present (BP).*

Core	Dated material	^{14}C age	Cal. yr. BP.
1070	Bivalve shell fragments, depth 316 cm	14 680 +/- 40 (Yao et al., 2020)	17 067

Dated material was chosen and picked by Dr Haoyi Yao. Measurement was carried out with the AMS at the Beta Analytic Radiocarbon Dating facilities in Miami (US). The age of the sediment was calibrated using CALIB 8.20 software (Stuiver et al., 1993) and by applying the Marine20 calibration curve (Heaton et al., 2020) with 1R (marine reservoir age) = 0±50, as recommended by Andrews et al. (2016). The date is presented in calibrated years before present (ka cal BP), where zero-year BP is 1950 CE. (Table. 5)

3.2.1 Subjective abundancy of foraminifera

The subjective abundancy of the planktic and benthic (both calcareous and agglutinated) foraminifera were studied using stereomicroscope at the IG, UiT. Every 5-cm interval was investigated. The abundancy of each foraminiferal group was defined with the abundancy scale of 0 – 5 with the following determinations: 0 (absent), 1 (rare), 2 (present), 3 (some), 4 (abundant), 5 (very abundant).

3.2.2 Ice rafted detritus (IRD)

The IRD content of the sediments was investigated by following the method introduced by Grobe (1987). The gravel size fraction (>2 mm) clasts were counted from every 1-cm thick horizon in the X-radiographs. Possible enrichments of gravel size clasts caused by bioturbation and methane-derived authigenic mineral precipitations were not counted. Clasts extending equally into two distinct horizons were counted as belonging to the upper horizon.

3.2.3 Lithological description

The core surfaces were studied for the lithological description at the IG, UiT in 2019. The cores were opened earlier in 2016. Lithology log was made by studying the X-ray images and the sediment surfaces of the archive halves (the archive half of the #2, core 1069, was damaged (appendix) so the working half was used here instead). The color, lithological composition, sedimentary structures, and the presence of macrofossils were described. Before studying the sediment surfaces, the top layer of the sediment surface was removed carefully to expose the unoxidized sediment surface. Then the surfaces were carefully smoothed with a plastic card to reveal its physical characteristics. To prevent contamination a) the smoothing was done perpendicular to the long core axis, b) the plastic card was cleaned between every wipe.

The content of unidentified clast with a size of 5 x 2.5 cm from the top of the core 1070 (Fig. 9) was tested with the “acid test”. A drop of hydrochloric acid (HCL, 5%) was dropped on the surface of the clast. If the clast is calcium carbonate CO_2 is formed.

3.2.4 Grain size analysis

The grain size analysis was based on the residue weights (g) of wet sieved sediment samples. The measured grain sizes were >250mm, 100 – 250 mm (fine sand) and 63 – 100 mm (very fine sand). Measurement was performed every 10 cm along the cores. The classification of the sediment grain sizes was based on Udden (1914) and Wentworth (1922).

3.2.5 Visual investigation, SEM (*scanning electron microscope*), and EDS (*Energy-Dispersive X-Ray Spectroscopy*)

For the visual investigations, specimens from depth intervals with strongly depleted and normal $\delta\ ^{13}C$ values were selected. Investigated species were *N. pachyderma, C. neoteretris and C. reniforme* (Table. 6). The $\delta\ ^{13}C$ values representative for non-seep environments, are considered

to be between -0.5 and 0.5‰ for *N. pachyderma* (Zamelczyk et al., 2014; Werner et al., 2016), and between −0.3 ‰ to −1 ‰ for *C. neoteretis* (Wollenburg et al., 2001).

Table 6. *SEM-EDS investigations: foraminifera species, δ ^{13}C values, depth, and core.*

Core	Depth (cm)	Species	δ ^{13}C value (‰)
1070	156 – 157	*C. neoteretis*	- 1.14
1070	286 – 287	*C. neoteretis*	- 11.34
1070	286 – 287	*N. pachyderma*	- 8.26
1069	11 – 12	*C. reniforme*	- 10.16
1069	88 – 89	*C. reniforme*	- 1.87
1069	116 - 117	*N. pachyderma*	0.14

Specimens were photographed using Leica DFC 450 digital camera mounted on a Leica Z16 Apo stereomicroscope and described (colour, texture, transparency, reflectance, and morphological features). Then the tests were placed on adhesive tape and coated with fine carbon layer to enable good image resolution for the scanning electron microscope investigation (SEM).

SEM in conjunction with the Energy-Dispersive X-Ray Spectroscopy (EDS) enabled investigation of the nano-scale microstructural features on surface of foraminiferal tests. Investigation was performed using SEM Hitachi Tabletop Microscope TM-3000 and SEM Carl Zeiss LEO 1450VP and Quantax 70 software at the IG, UiT. In particular interest was the distribution and abundance of the element Magnesium (Mg), an indicative element of methane-induced diagenetic alteration on test (Aloisi et al., 2000; Naehr et al., 2007).

Results were described by using the terminology (“glassy” and “frosty”) by Sexton et al., (2006). Diagenetic alteration stages (“pristine”, and “minor-, moderate- or major diagenetic alteration”) of the tests were defined by the criteria developed by Schneider et al., (2017).

4 Results

4.1 Modern oceanography

Within the uppermost ~15 m of the water column, the temperature is constant ~ 6.5°C. A sharp temperature gradient is observed between the depths of ~ 24m and 30m; temperature decreases from 6.5°C to 5.5°C within six meters. From ~ 30m to ~ 350m, gradually 3.1°C from 5.5°C to 2.4°C. Temperature remains constant at 2.4°C within the lowermost ~ 30m of the water column. In total, the temperature decreases 4.1°C through the whole water column (380m) from the sea surface (~ 6.5°C) to the sea bottom (2.4°C) (Fig. 6).

Within the uppermost ~ 15m of the water column the salinity remains stable at 35.10 psu. Varying values are observed from ~ 15m to ~ 26m; the salinity varies between 35.10 psu and 35.14 psu. From ~ 26m salinity starts to decrease gradually. Within the lowermost ~ 30m from ~ 350m to ~ 380m salinity remains constant at ~ 34.96 psu. In total, the salinity decreases 0.14 psu through the whole water column (380m) (Fig. 6).

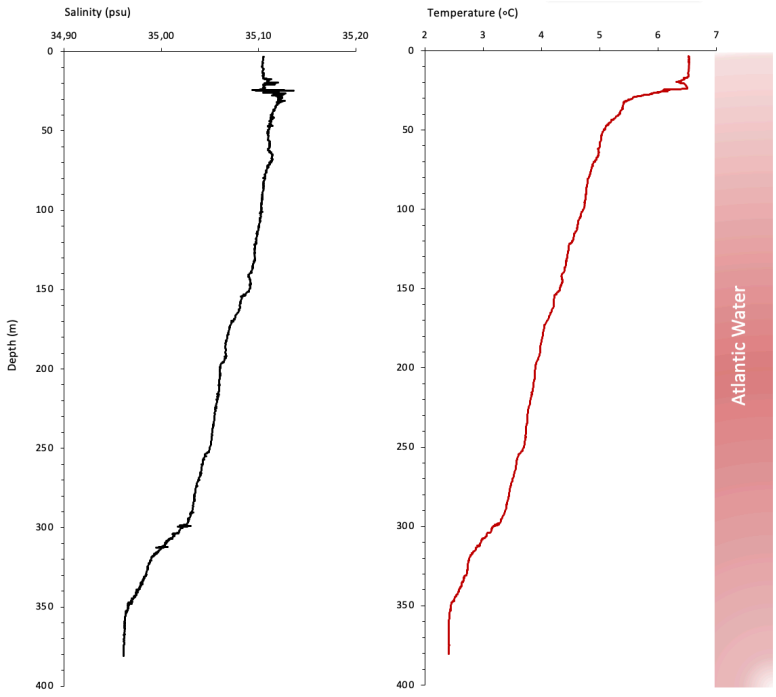

Figure 6. *CTD profile of salinity and temperature (June 2016) from the CTD-station CAGE 16-5 HH 1046, above Pingo 5.*

4.2 Age model and sedimentation rate

The chronostratigraphic framework of this study is based on one AMS ^{14}C age from the core 1070 (depth 316 – 317 cm) (Yao et al. 2020), and on lithostratigraphic correlation to two AMS ^{14}C ages published by Jessen et al. (2010). The two ^{14}C ages from Jessen et al. (2010) corresponds to the two tie points from the lower and upper boundaries of the diatom rich layer. These dates are regarded as chronostratigraphic markers for the western Svalbard slope. The correlated diatom rich layer is found from the core 1070 between 76 – 100 cm bsf (Fig. 7, 13).

Table 7.*The chronostratigraphic framework: one AMS ^{14}C age and lithostratigraphic correlation to two AMS ^{14}C ages published by Jessen et al. 2010.*

Core	Source	^{14}C age	Cal. yr. BP.
1070	The upper boundary of the diatom rich layer, depth 76 cm	8800 +/- 100 (Jessen et al., 2010)	9370
1070	The lower boundary of the diatom rich layer, depth 100 cm	8950 +/- 100 (Jessen et al., 2010)	9599
1070	Bivalve shell fragments, depth 316 cm	14 680 +/- 40 (Yao et al., 2020)	17 067

The radiocarbon ages were calibrated using CALIB 8.20 software (Stuiver et al., 2020) and by applying the Marine20 calibration curve (Heaton et al., 2020) with 1R (marine reservoir age) = 0± 50, as recommended by Andrews et al. (2016). The date is presented in calibrated years before present (ka cal BP), where zero-year BP is 1950 CE (Table. 7).

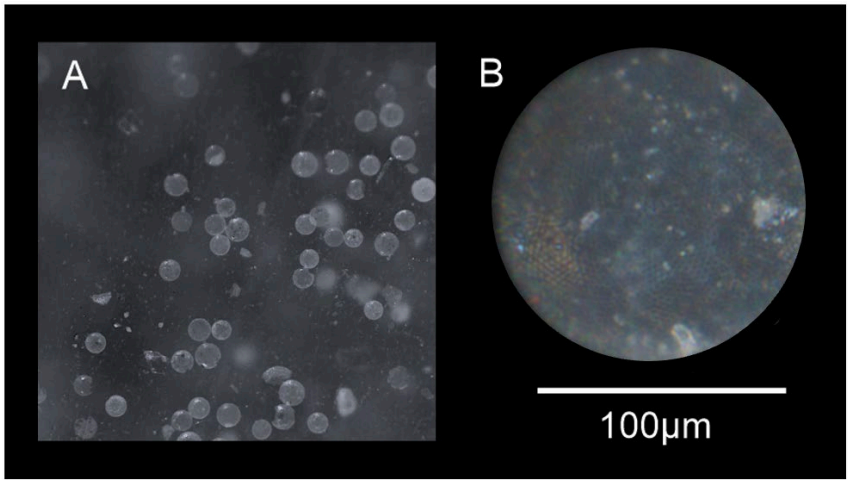

Figure 7. (A) *General view of the diatom rich layer (76 – 100 cm) seen in the very fine sand fraction through stereomicroscope.* ***(B)*** *The Diatom rich layer is dominated by Coscinodiscus spp.*

According to the estimated AMS-^{14}C age from the oldest sediments in the core 1070 the record comprises the time period of ~ 17 067 cal. yr. BP years to present, comprising the Heinrich stadial HS1 (17 500 – 14 600 cal years BP), Bølling and Allerød interstadials (14 600 – 12 800 cal years BP), the Younger Dryas stadial (12 800 – 11 700 cal years BP), and the Holocene epoch (11 700 cal years BP - present).

Any AMS ^{14}C dates are not measured for the core 1069. In addition, stratigraphic correlation to other data is challenging as the diatom rich layer is not found, the δ^{18}O is measured only within the topmost ~120 cm (as the foraminifera are absent below this depth), and the δ^{18}O record has a measuring interval of 10 cm (Fig. 16). Caused by these reasons, it is challenging to try to establish any age model for the core 1069. However, the laminated interval was found between ~186 - 210 cm most likely representing the well-known distinct lithological shift in the sedimentological records of Storfjorden Trough and in the whole Barents Sea region (Fig. 14 and 15) (Svendsen et al., 1996; Aagaard-Sørensen et al., 2010; Jessen et al., 2010; Junttila et al., 2010; Nielsen and Rasmussen, 2018; Rasmussen and Thomsen, 2021). The relatively consistent ages obtained above and below the laminated interval have indicated that the layer has been deposited around 14,400 cal years BP corresponding to the Bølling interstadial (Jessen et al., 2010; Rasmussen and Thomsen, 2021). The laminated interval was not found from the core 1070 (Fig. 10 and 12).

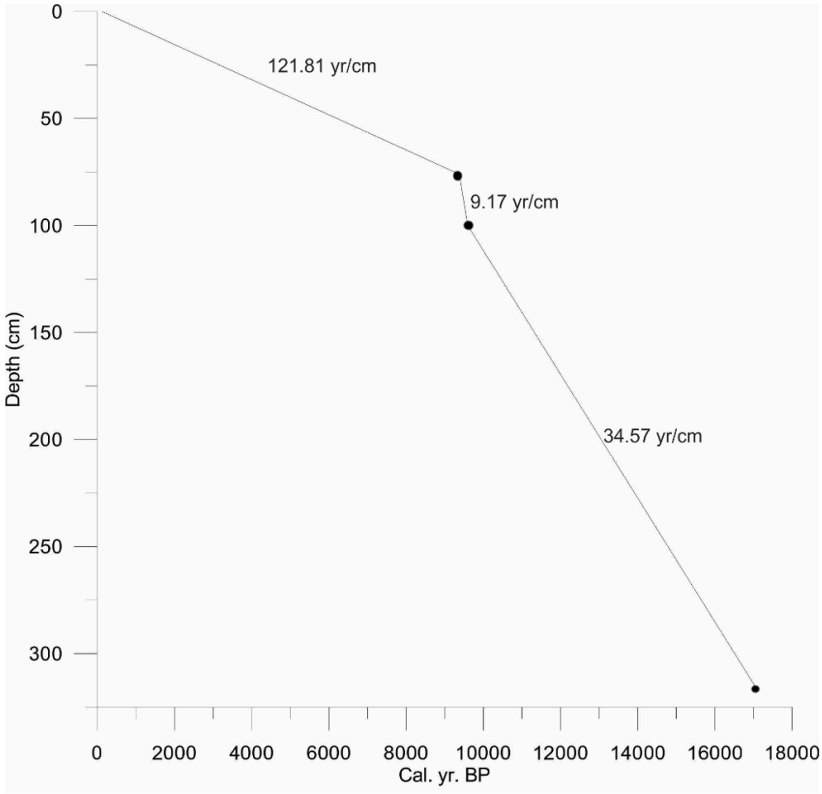

Figure 8. *Calculated average sedimentation rate for the core 1070.*

Calculated sedimentation rate for the core 1070 is the highest within the interval between 9379 – 9599 cal. yr. BP where it has taken 9.17 years for 1 cm to accumulate. The lowest calculated sedimentation rate is found within the first 9379 cal. yr. BP (121.81 yr/cm). During the interval of 9599 – 17 067 cal. yr. PB the calculated sedimentation rate is 34.57 yr/cm (Fig. 8).

4.3 Core 1070

4.3.1 Isotopic signature

The $\delta^{13}C$ signature measured in tests of *Cassidulina. neoteretis* vary from -1.10 to -11.34‰. The lowest values are found at 26 cm (-4.34‰), between 186 – 257 cm (-4.25 to -11.03‰) and at 286 cm (-11.34‰). Elsewhere, the values remain relatively stable from -1.10 to -3.34‰ (Yao et al., 2020*)* (Fig. 13).

The $\delta^{13}C$ signature of *Neogloboquadrina pachyderma* vary from 0.37 to -8.26‰. The lowest values are found within the topmost 27 cm (from -3.02 to -5.87‰), at 126 cm (-1.08‰), between 186 – 207 cm (from -1.57 to -6.56‰), at 226 cm (-2.94‰), and below 276 cm (from -1.11 to -8.26‰). Elsewhere, the values remain relatively stable from 0.37 to -0.96‰ (Yao et al., 2020*)* (Fig. 13).

The ice volume corrected $\delta^{18}O$ signature of *C. neoteretis* has an increasing trend towards the core top. The values vary between 2.35 – 4.66‰. Within the topmost 77 cm the values are generally higher and more stable than deeper in the core. The highest value is found at 66 cm (4.66‰). The lowest values are found at 256 and 316 cm with values of 2.41 and 2.35‰ respectively (Fig. 13).

The uncorrected $\delta^{18}O$ signature of *C. neoteretis* varies between 3.48 and 4.89‰. The lowest values are found at 256 and 316 cm with values of 3.48 and 3.52‰ respectively. The highest value is found at 66 cm (4.89‰) and at 206 cm (4.88‰) (Fig. 13).

The ice volume corrected $\delta^{18}O$ signature of *N. pachyderma* varies between 2.52 – 3.65‰. Within the topmost 77 cm the values are generally higher and more stable than deeper in the core. The highest value of the record is found here at 66 cm (3.65‰) (Fig. 13).

Below 77 cm the values remain mainly below 3‰. The lowest values are found from at 116 (2.52‰) and 206 cm (2.62‰). At 126, 176, 196, and 316 cm the values increase slightly above 3‰. High peak value is found at 236 cm (3.62‰) (Fig. 13).

The uncorrected $\delta^{18}O$ signature of *N. pachyderma* varies between 2.96 and 4.66‰. Decreasing trend is observed towards the core top. The lowest values are found at 116 cm (2.96‰). The highest value is found at 236 cm (4.66‰) (Fig. 13).

4.3.2 Magnetic susceptibility

Magnetic susceptibility record of the core 1070 varies from 7.67 to 32.75 SI with an average value of 11.3. Within the bottommost 25 cm between 295 to 320 cm the values are characterized by an increasing trend towards the core top. Between 210 and 295 cm the values fluctuate strongly. Peak values are observed at 290 and 245 cm with values of 33 and 22 SI respectively. The topmost 210 cm is characterized by relatively stable values with an average value of 10.4 SI (Yao et al., 2020) (Fig. 13).

4.3.3 IRD, grain sizes and lithostratigraphy

The topmost ~150 cm of the core 1070 consists of structureless dark brown mud. The IRD is mainly absent, only few drop stones are found occasionally. Within the topmost ~30 cm the mud is crudely bedded with sand fraction size sediment (Fig. 10). The unknown clast on top of the core was identified as calcium carbonate (Fig. 9, 10). Between ~20 and 50 cm, dark, dense, and small grains, interpreted as authigenic precipitation, are found scattered throughout the sediment (Fig. 11). Bivalves are found occasionally throughout the sediment and especially between ~85 and 150 cm where they are accompanied with bioturbation (Fig. 10).

Within the bottommost ~170 cm (150 – 320 cm) IRD-rich layers and structureless mud alternate with each other. The first IRD-rich layer is found between 150 – 163 cm. The angular clasts without long axis orientation are found from dark brown muddy matrix. A peak in > 250μm grain size fraction is observed at 160 cm. The IRD-rich layer is followed by a layer of mud layer between 163 – 188 cm. The layer consists occasional angular drop stones. The color of the layer alternates from light reddish brown to light grey, seen as alternating darker and lighter beds in x-ray image (Fig. 10).

A 5 cm thick IRD-rich layer is observed between 188 – 193 cm. The clasts are angular, and they do not have long axis orientation. The matrix is dark brown mud. The layer is accompanied with peak value of >250 μm grain size fraction at 190 cm (Fig. 11). Structureless dark brown mud with few angular drop stones is found between 193 – 199 cm (Fig. 10,).

The next IRD-rich layer is found between 199 – 211 cm. The angular clasts do not have long axis orientation. The matrix is dark brown mud. The layer is accompanied with peak value of

>250 µm grain size fraction at 210 cm. A layer of structureless dark brown mud is found between 211 – 219 cm. The layer is absent of drop stones. Some bioturbation is observed (Fig. 10, 12).

Two sharp IRD peaks are found at 220 and 222 cm with 11-12 clasts within 1 cm horizon. These peaks are accompanied with peak value in >250 µm grain size fraction at 220 cm. The angular IRD clasts have no long axis orientation. The IRD-rich layer is followed by structureless dark brown mud between 224 – 229 cm (Fig. 10, 12).

The next IRD-rich layer is found between 229 – 235 cm. Angular IRD clasts have no long axis orientation. The layer is followed by a thick layer (40 cm) of structureless dark brown mud between 235 and 264 cm. The layer contains occasional drop stones and some bioturbation and a bivalve (Fig. 10, 12).

A 30 cm thick layer of angular IRD is found between 264 – 306 cm. The clasts have no long axis orientation, and some clasts are relatively large; up to 4 cm in diameter. A sharp IRD peak is found at 282 cm with 16 clasts per 1 cm horizon. Few bivalves are found within the bottommost part of the layer with fewer IRD. The matrix is dark brown mud. The bottommost 14 cm of the core consists of structureless dark brown mud with few bivalves (Fig. 10, 12).

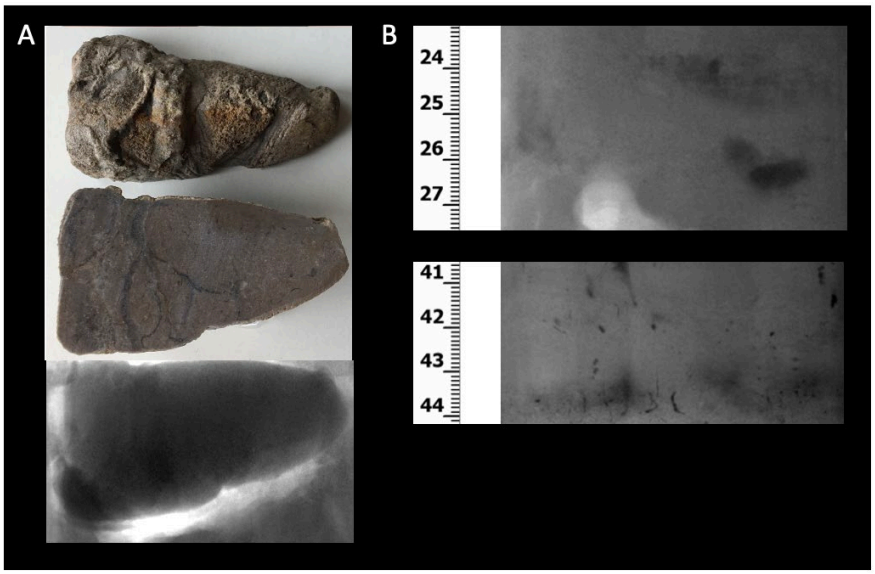

Figure 9. *Core 1070:* ***A)*** *Piece of calcium carbonate crust on top of the core, depth: 0-3 cm. On top: external surface, in the middle: splitted surface, at the bottom: X-ray image,* ***B)*** *X-ray image of dark, and dense precipitation scattered throughout the sediment within the barite fronts around 25 and 42 cm.*

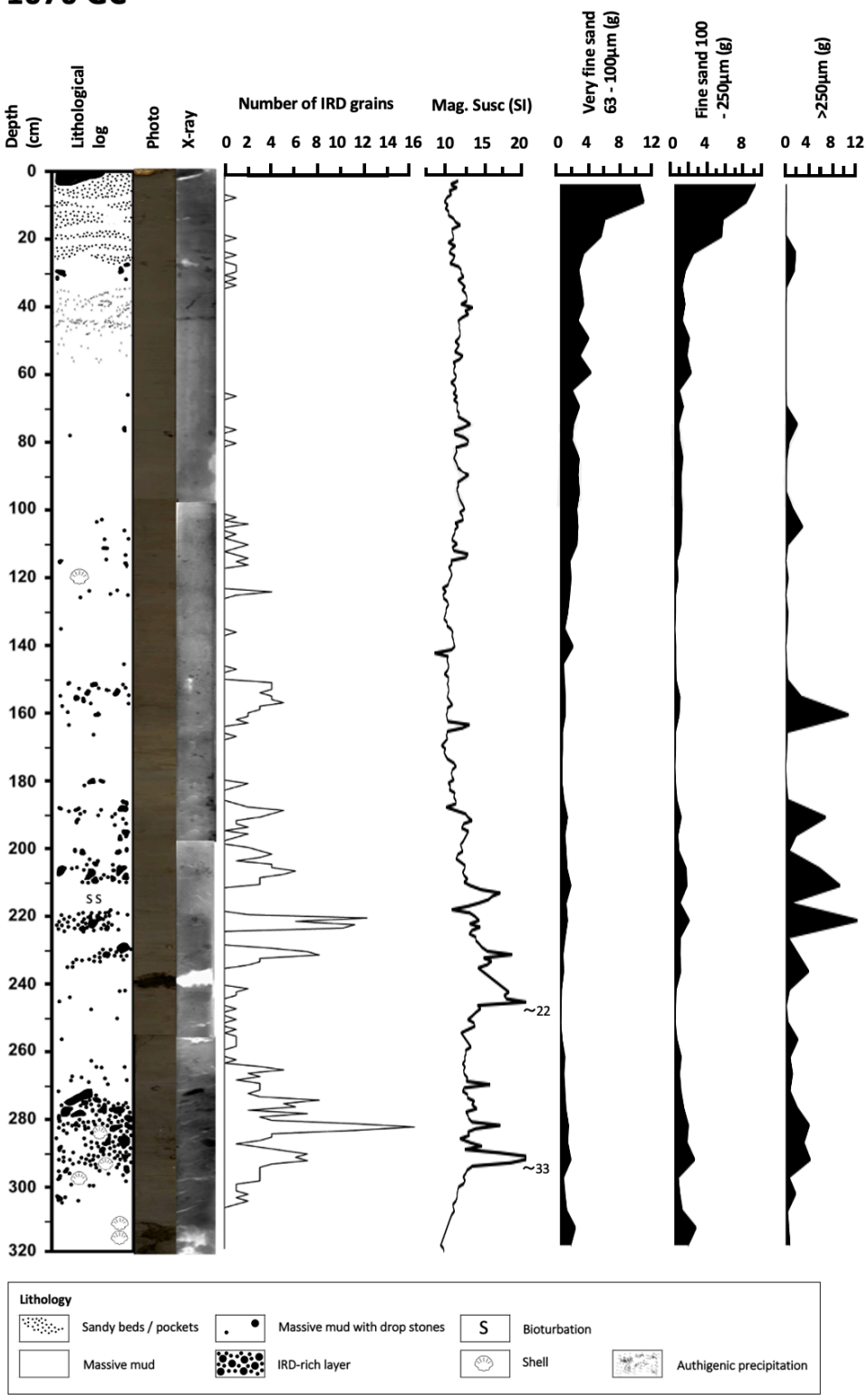

Figure 10. *Core 1070, from left: lithology log, photo, X-ray image, IRD-, Magnetic Suceptibility-, and grain size records.*

4.3.4 Subjective abundancy of foraminifera

The core 1070 is almost barren of agglutinated foraminifera. They are observed only from two distinct depths at 166 and 221 cm as 1/rare (Fig. 13). Planktic foraminifera are found with the scale of 1/rare – 3/some. For most of the core they are found as 1/rare. At three horizons they reach abundancy of 3/some: at 186 – 201 cm, 226 and 311 cm. They are absent at several horizons between 101 – 271 cm. Between 246 – 271 cm they are mostly absent. Other depths with absence are: 101, 121, 131, 141, 171, 211, and 221 cm (Fig. 13). Benthic foraminifera are present throughout the core and found as 1/rare – 4/abundant. They are found as 4/abundant within eight horizons throughout the core: 6 - 11, 21, 76, 151 – 161, 186 – 191, 226, 266 and 296, - 301 cm. They are found as 1/rare only from three horizons at 66, 181 and 221 cm (Fig. 12).

4.3.5 XRF

The solid phase elemental composition of the core 1070 is described below with downcore profiles of S/Rb, Ba/Rb, P/Rb, Mn/Rb and Fe/Rb.

The S/Rb ratio fluctuates strongly between 0.1 – 1.5 and many peaks are observed throughout the core. The average value is 0.7. Increasing trend towards the core top is observed above 98 cm (Fig. 11).

The Ba/Rb ratio has nearly constant values throughout the core between -0.04 and 1.3. The average value is 0.3. Within the topmost 27 cm the ratios are slightly higher than deeper in the core. Distinct peaks are observed at 26, 41, 50, and 255 cm with values of 0.7, 1.3, 0.7 and 0.8 respectively (Fig. 11).

The P/Rb ratio fluctuates strongly throughout the core between -3.2 and 0.4 and with average value of -1.1. Two distinct peaks are observed at 236 and 255 cm with values of 0.4 and 0.1 respectively (Fig. 11).

Relatively stable values between -0.9 and 1.6. characterize the Mn/Rb record. The average value is 0.0. Distinct peaks are observed at 236, 255, 310 and 318 cm with values of 1.6, 1.6, 1.1 and 0.9 respectively (Fig. 11).

The Fe/Rb ratio is characterized by stable values from -1.1 to 3.7 throughout the core. The average value is 2.0. Two peak values are found at 235 and 264 cm with values of 3.7 and 3.5 respectively (Fig. 11).

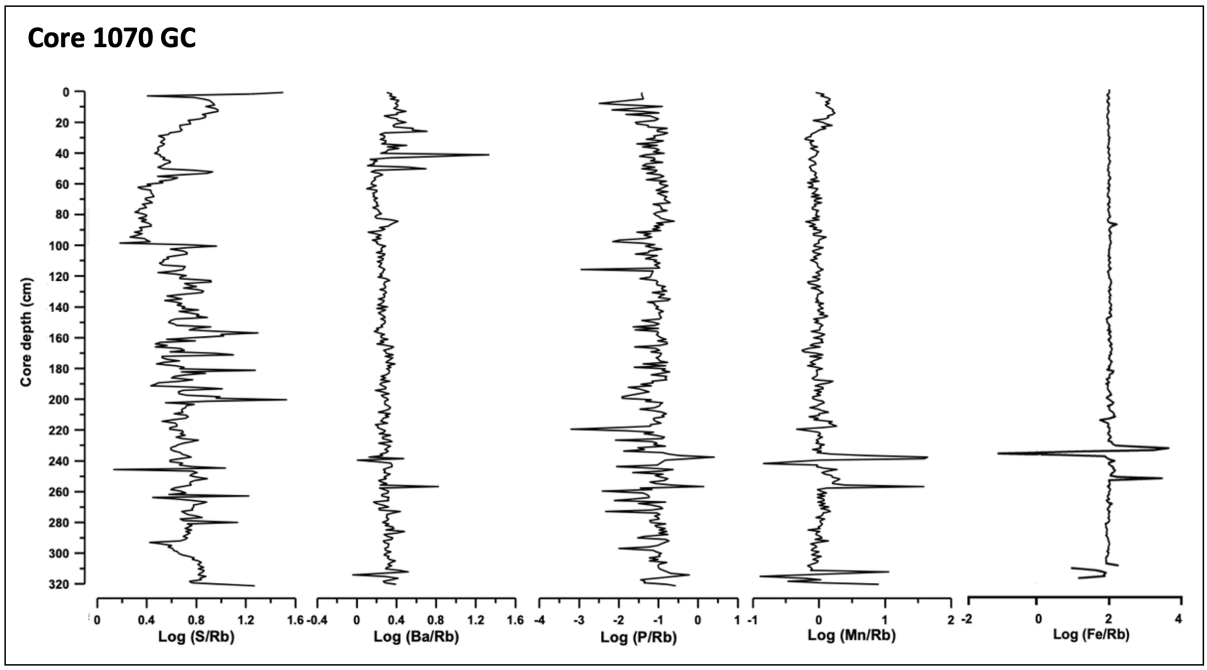

Figure 11. *Core 1070, solid state elemental composition: Sulfur (S), Barium (Ba), Phosphorous (P), Manganese (Mn,) and Iron (Fe) normalized against Rubidium (Rb).*

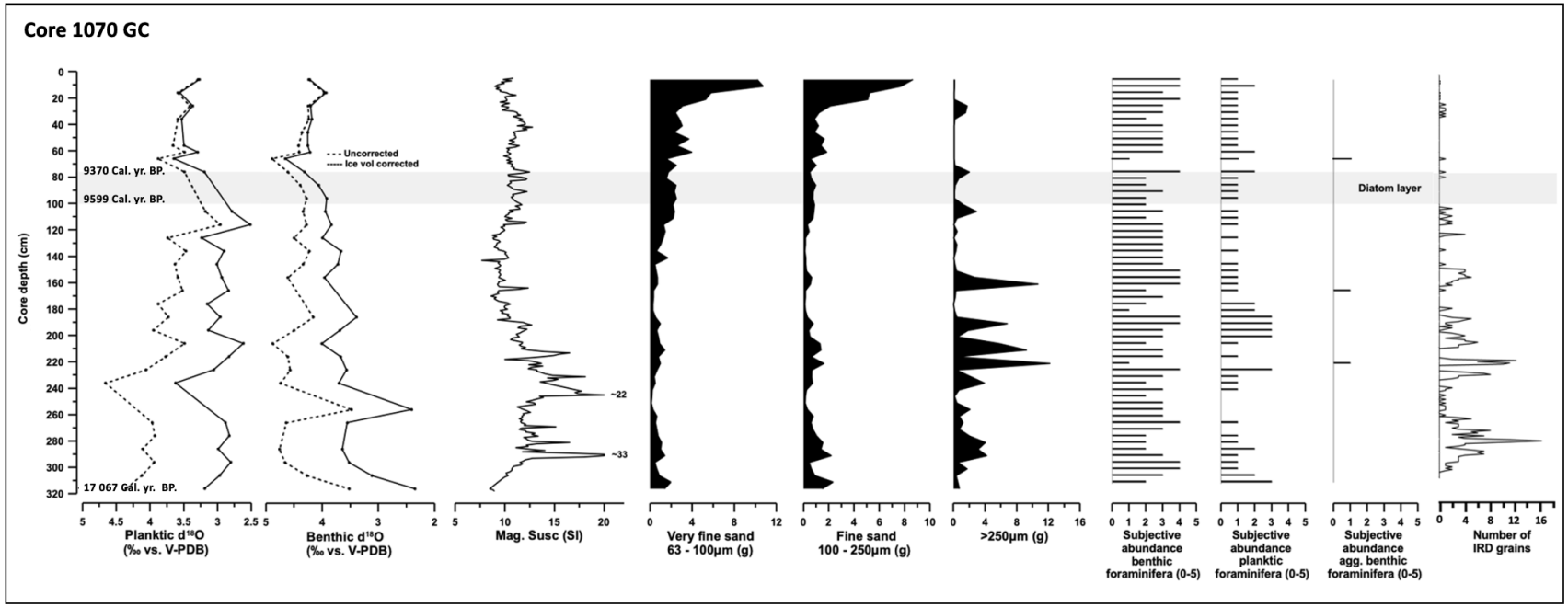

Figure 12. *Various proxies from the core 1070: the stable isotopic record of δ13C and δ18O, magnetic susceptibility, grain size fractions, subjective abundance of benthic, planktic and agglutinated foraminifera and the ice rafter debris. Diatom rich layer is indicated with grey color.*

4.4 Core 1069

4.4.1 Isotopic signature

The $\delta^{13}C$ signature of *Cassidulina reniforme* is measured from the topmost 107 cm of the core, where the benthic foraminifera are present. The $\delta^{13}C$ signature of *C. reniforme* vary from -1.66 to -10.16‰. The lowest values are found within the topmost 19 cm (from -4.78 to -10.16‰), at 51 cm (-8.98‰) and at 71 cm (-5.26‰). Elsewhere, the values remain relatively stable from -1.66 to -2.85‰ (Fig. 18).

The $\delta^{13}C$ signature of *N. pachyderma* is measured from the topmost 117 cm of the core, where the planktic foraminifera are present. The values vary from -0.41 to -5.81‰. The lowest values are found within the topmost 19 cm (from -1.53 to -2.20‰), at 51 cm (-1.91‰), and within 71 – 79 cm (from -1.29 to -5.81‰). Elsewhere the values remain relatively stable from -0.41 to -0.57‰ (Fig. 18).

The $\delta^{18}O$ signature of *C. reniforme* is measured from the topmost 107 cm of the core, where the benthic foraminifera are present. The values vary between 4.42 and 4.82‰. The lowest values are found at 31 and 106 cm with values of 4.47 and 4.42‰ respectively. The highest values are found at 58 and 71 cm with values of 4.77 and 4.82‰ respectively (Fig. 18).

The $\delta^{18}O$ signature of *N. pachyderma* is measured from the topmost 117 cm of the core, where the planktic foraminifera are present. The values vary between 2.57 and 4.83‰. Most of the samples has a value > 3‰. The lowest value is found at 31 cm (2.57‰). The highest $\delta^{18}O$ values are found at 58 and 72 cm with values of 4.83 and 4.12‰ respectively (Fig. 18).

4.4.2 Magnetic susceptibility

The magnetic susceptibility record of the core 1069 varies from 8.86 to 15.74 SI. The average value is 10.7. The record has gradually decreasing trend towards the core top. Two peak values are observed at 1 and 95 cm with values of 15.4 and 15.7 SI respectively (Fig. 18).

4.4.3 IRD, grain sizes and lithostratigraphy

The topmost 135 cm of the core 1069 is consisted of dark brown mud and the topmost 75 cm of it is crudely bedded with sand fraction size sediment. IRD is mostly absent, some drop stones are observed occasionally. High peak in >250 μm grain size fraction is observed at 50 cm. Between ~43 - 50 cm small, dense, and dark grains are found scattered throughout the sediment (Fig. 14). Occasional bivalves and bioturbation are found from the topmost ~110 cm. Many

bivalves are found between 110 – 120 and the bioturbation is common between 107 – 135 cm (Fig. 15, 18). A layer of angular IRD is found between 134 – 155 cm. The clasts have no long axis orientation. The clasts become more abundant towards the core top with a peak of 9 clasts at 137 cm. The matrix is dark brown mud (Fig. 15, 18). The IRD rich layer is followed by a layer of structureless mud between 155 – 170 cm. A distinct clast with a size of ~5.5 x 2.5 cm is found at 159 cm (Fig. 13). It is characterized by rusty iron color and mineral fragments with brass-yellow color and metallic luster. A peak in >250 μm grain size fraction is found at 160 cm. The topmost part of the mud layer has dark brown color whereas between 165 – 188 cm the color alternates from light reddish brown to light grey (Fig. 15, 18). Between 170 – 181 cm a layer of angular IRD is observed. The clasts have no long axis orientation. The layer is followed by structureless mud between 181 – 186 cm. One drop stone and one bivalve are found (Fig. 15, 18).

Laminated mud is found in X-ray images between ~186 and 210 cm. Sharp IRD peak of 11 clasts is found at 190 cm. Some bioturbation is observed at the top of the layer. Few drop stones are found within the lamination. The bottommost ~10 cm is consisted of structureless mud with few drop stones and a bivalve (Fig. 15, 18).

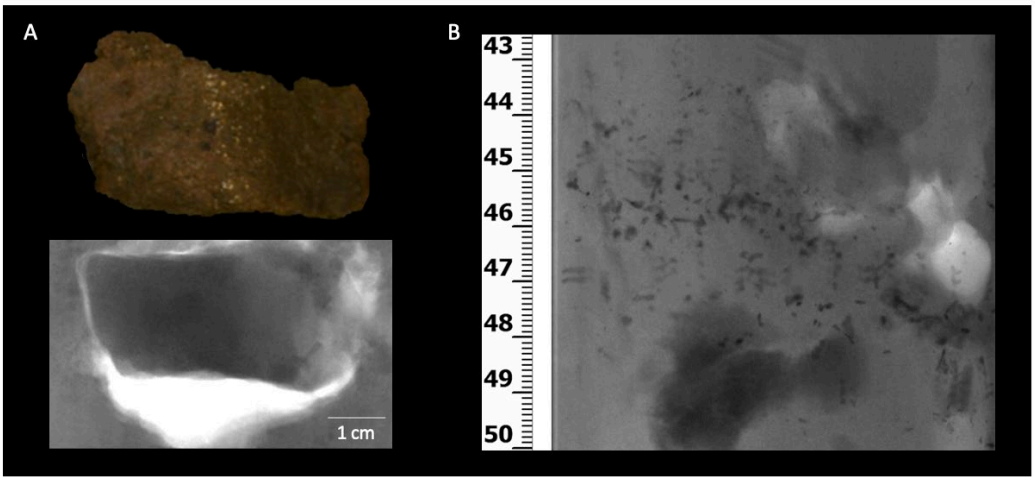

Figure 13. *Core 1069**: A)** Pyrite block, depth ~160 cm. On top: photo, at the bottom seen in X-ray image, **B)** X-ray image of dark, and dense precipitation scattered throughout the sediment within the barite front, between 43-50 cm.*

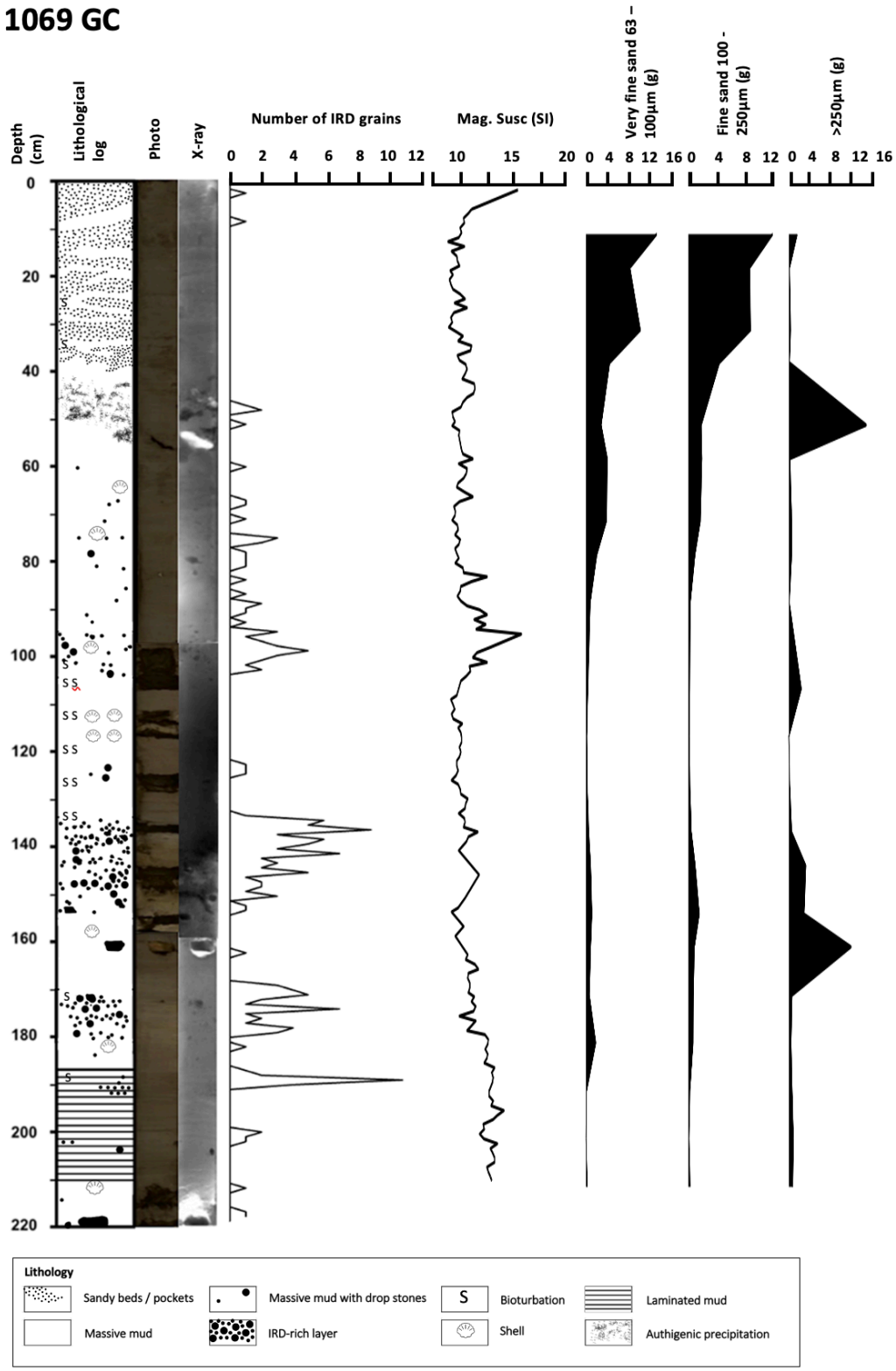

Figure 14. *Core 1069, from left: lithology log, photo, X-ray image, IRD-, Magnetic susceptibility-, and grain size records.*

4.4.4 Subjective abundancy of foraminifera

The core 1069 is almost barren of agglutinated foraminifera. They are found only from two distinct horizons at 51 – 58 cm and 126 cm as 1/rare (Fig. 18). Planktic foraminifera are absent below 117 cm. Between 31 – 117 cm they are found as 1/rare. Within the topmost 18 cm they are found as 2/present (Fig. 18). Benthic foraminifera are absent below 144 cm and at 136 cm. Between 38 and 126 cm they are found either as 2/present or as 3/some. They are most abundant within the uppermost 32 cm as 4/abundant - 5/very abundant (Fig. 18).

4.4.5 XRF

The solid phase elemental composition of the core 1069 is described below with downcore profiles of S/Rb, Ba/Rb, P/Rb, Mn/Rb and Fe/Rb. The S/Rb ratios vary from 0.3 to 2.0 with average value of 0.8. The values vary stronger within the bottom half of the core with observed peak value of 2.0 at 164 cm. Above 100 cm the overall trend is slightly increasing (Fig. 17). The Ba/Rb record remains nearly constant throughout the core with values from -2.2 to 0.8. The average value is 0.2. Strong negative peak is observed at 160 cm with value of -2.2. Two small peaks are observed at 49 and 219 cm with values of 0.8 and 0.5 respectively (Fig. 17). The P/Rb record varies between 1.3 and 3.7 with average value of 3.5. Distinct negative peaks are observed at 55, 145, 165 and 219 cm with values of 3.0, 2.9, 2.8 and 1.3 respectively (Fig. 17). Relatively stable values from -0.3 to 0.9 characterize the Mn/Rb record with average value of 0.0. Distinct peaks at 151, 163 and 219 cm are observed with the values of 0.6, 0.4 and 0.9 respectively (Fig. 17). The Fe/Rb values vary between 0.9 and 2.7. The average value is 2.0. One peak value is found at 163 cm (2.7).

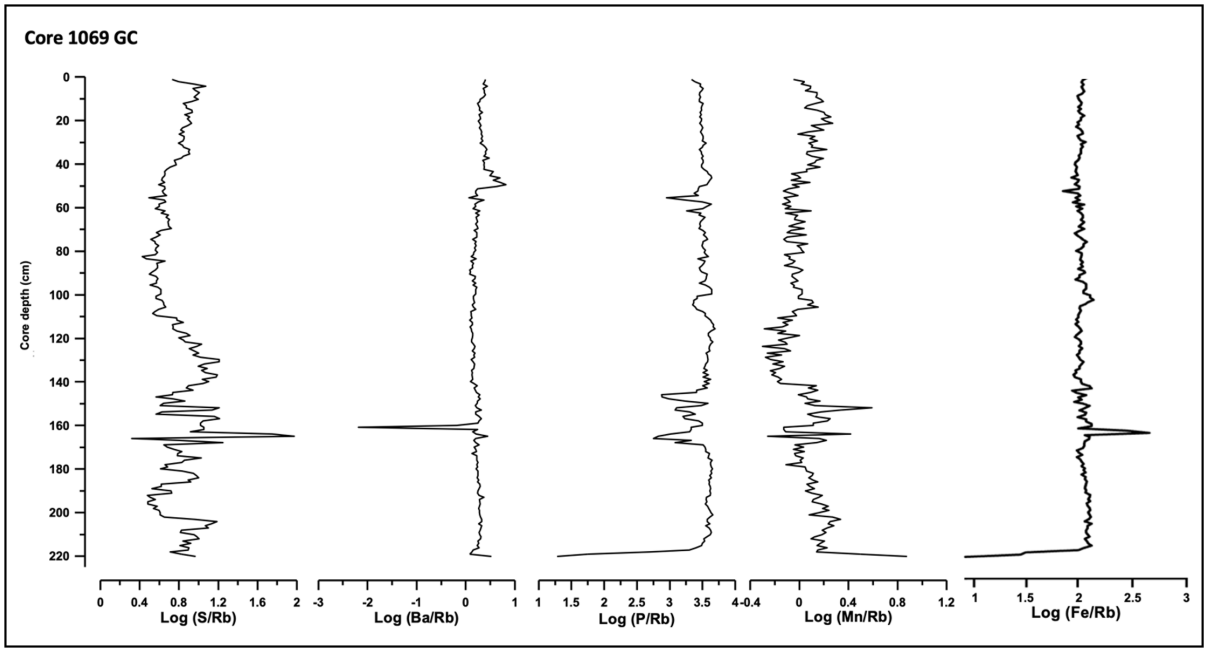

Figure 15. *Solid state elemental composition of the core 1069. Sulfur (S), Barium (Ba), Phosphorous (P), Manganese (Mn,) and Iron (Fe) are normalized against Rubidium (Rb).*

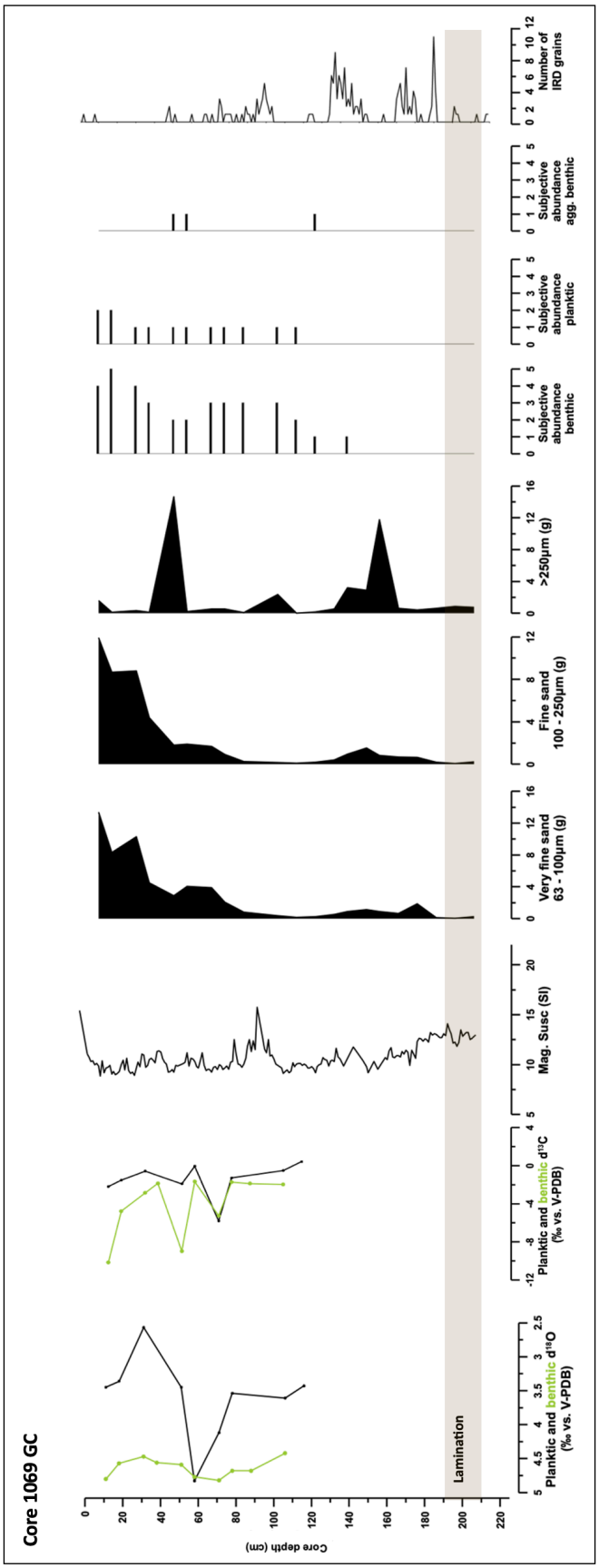

Figure 16. *Various proxies from the core 1069: the stable isotopic record of δ13C and δ18O, magnetic susceptibility, grain size fractions, subjective abundance of benthic, planktic and agglutinated foraminifera and the ice rafter debris. Laminated layer is marked with brown bar.*

4.5 SEM – EDS

4.5.1 Cassidulina neoteretis

Benthic foraminifera species *Cassidulina. neoteretis* is studied with the following $\delta^{13}C$ values and depths from the core 1070:

- -1.14‰ (156 – 157 cm)
- -11.34‰ (286 – 287 cm)

C. neoteretis with the $\delta^{13}C$ value of -1.14‰ has transparent test with glassy appearance and high reflectance. The texture is optically smooth. Morphological features such as aperture, sutures and chambers are easy to observe under the stereomicroscope. SEM-EDS investigation does not reveal any foreign crystals or grains on the test and the pores are unplugged. Anomalous amounts of high-Mg calcite are not observed. The specimen is defined as ´pristine´(Fig.19).

The test of the *C. neoteretis* with the $\delta^{13}C$ value of -11.34‰ has a light grey – yellowish color under the stereomicroscope. The test is frosty, and it has lost its transparency, reflectance, and optically smooth texture. The SEM-EDS reveals plugged pores and widespread high-Mg Calcite crystals that have started to form solid crust on top of the exterior wall. The specimen is defined as having ´major diagenetic alteration´(Fig.19).

4.5.2 Neogloboquadrina pachyderma

Planktic foraminifera species *Neogloboquadrina pachyderma* is studied with the following $\delta^{13}C$ values, depths, and cores:

- 0.41‰ (116 – 117 cm, core 1069)
- -8.26‰ (286 – 287 cm, core 1070)

N. pachyderma with the $\delta^{13}C$ value of 0.41‰ has a test with grey color under the stereomicroscope. Morphological features such as aperture and champers recognizable. The SEM-EDS imagery reveals high-Mg calcite crystals covering the exterior wall. The pores are plugged. The specimen is however identified as `pristine´ according to its $\delta^{13}C$ value of 0.41‰ (Fig. 20).

The test of the *N. pachyderma* with the $\delta^{13}C$ value of -8.26‰ is white under the stereomicroscope. The test has a coarse texture. Morphological features such as chambers and aperture are recognized. The SEM-EDS imagery reveals pervasive high-Mg calcite crystals that have started to form solid crust on the exterior wall. The pores are plugged. The specimen is defined as having ´major diagenetic alteration´ (Fig. 20).

4.5.3 Cassidulina reniforme

Benthic foraminifera species *Cassidulina reniforme* from the core 1069, is studied with the following $\delta^{13}C$ values and depths:

- -1.87‰ (88 – 89 cm)
- -10.16‰ (11 – 12 cm)

C. reniforme with the $\delta^{13}C$ value of -1.87‰ has a highly transparent test with high reflectance and glassy appearance under the stereomicroscope. The texture of the test is optically smooth. Morphological features such as champers, sutures, and aperture are easily recognizable. The SEM-EDS imagery does not reveal foreign crystals or grains on the test and the pores are unplugged. Anomalous amounts of high-Mg calcite are not observed. The specimen is defined as ´pristine´ (Fig. 21).

The test of the *C. reniforme* with the $\delta^{13}C$ value of -10.16‰ has white-yellowish color. The surface of the test is grainy, and it has lost its transparency, reflectance, and optically smooth texture. Morphological features such as chambers and sutures are not distinguishable. The SEM-EDS imagery reveals pervasive and thick coating of crystals covering the exterior wall. The pores are plugged. The specimen is defined as having ´major diagenetic alteration´ (Fig. 21).

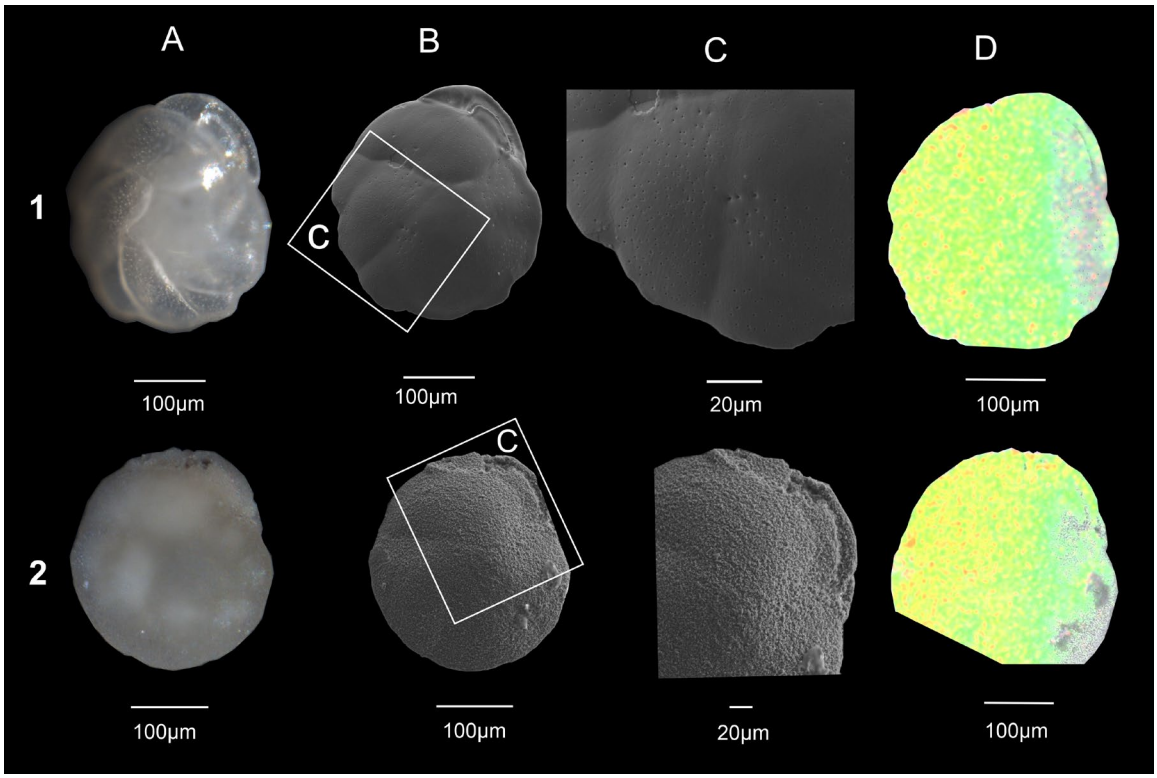

Figure 17. Row 1) *Pristine C. neoteretis with $\delta^{13}C$ value of 1.14‰,* ***Row 2)*** *C. neoteretis with major diagenetic alteration and $\delta^{13}C$ value of -11.34‰.* ***Columns: A)*** *The view through stereomicroscope,* ***B)*** *SEM image of the exterior wall,* ***C)*** *zoomed SEM image,* ***D)*** *EDS image. The color change in the EDS images from green to yellow and eventually to orange reflects the change in the Mg content in the test. Green = low content, yellow-orange = high content.*

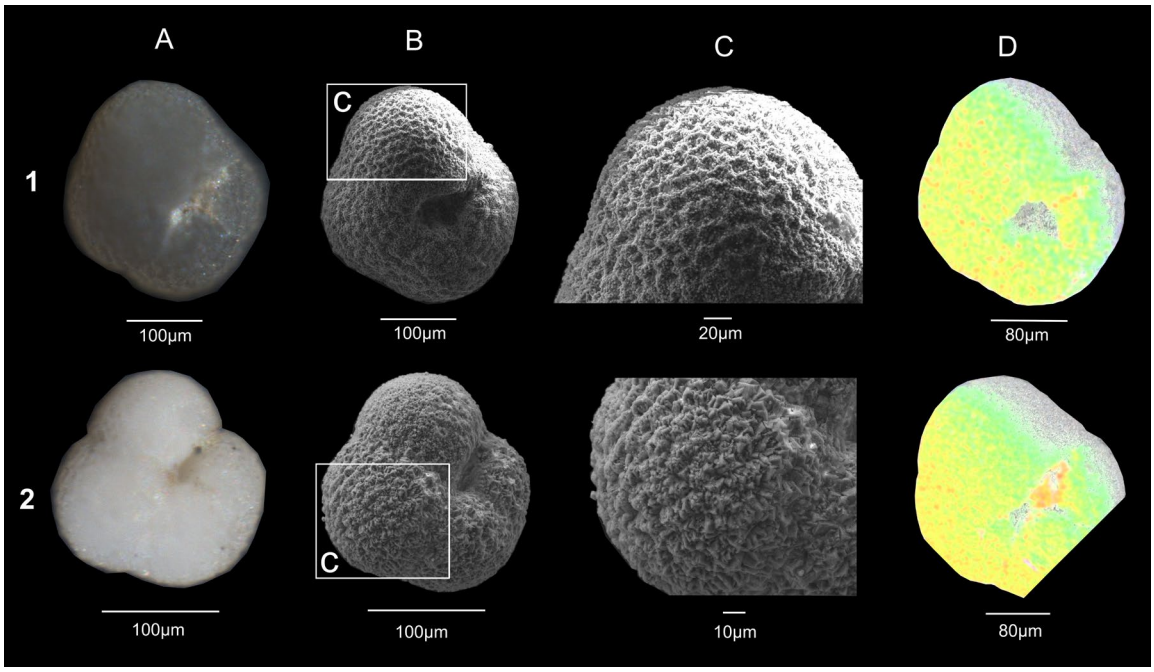

Figure 18. Row 1) *Pristine N. pachyderma with $\delta^{13}C$ value of 0.41‰,* ***Row 2)*** *N. pachyderma with major diagenetic alteration and $\delta^{13}C$ value of -8.26‰.* ***Columns: A)*** *The view through stereomicroscope,* ***B)*** *SEM image of the exterior wall,* ***C)*** *zoomed SEM image,* ***D)*** *EDS image. The color change in the EDS images from green to yellow and eventually to orange reflects the change in the Mg content in the test. Green = low content, yellow-orange = high content.*

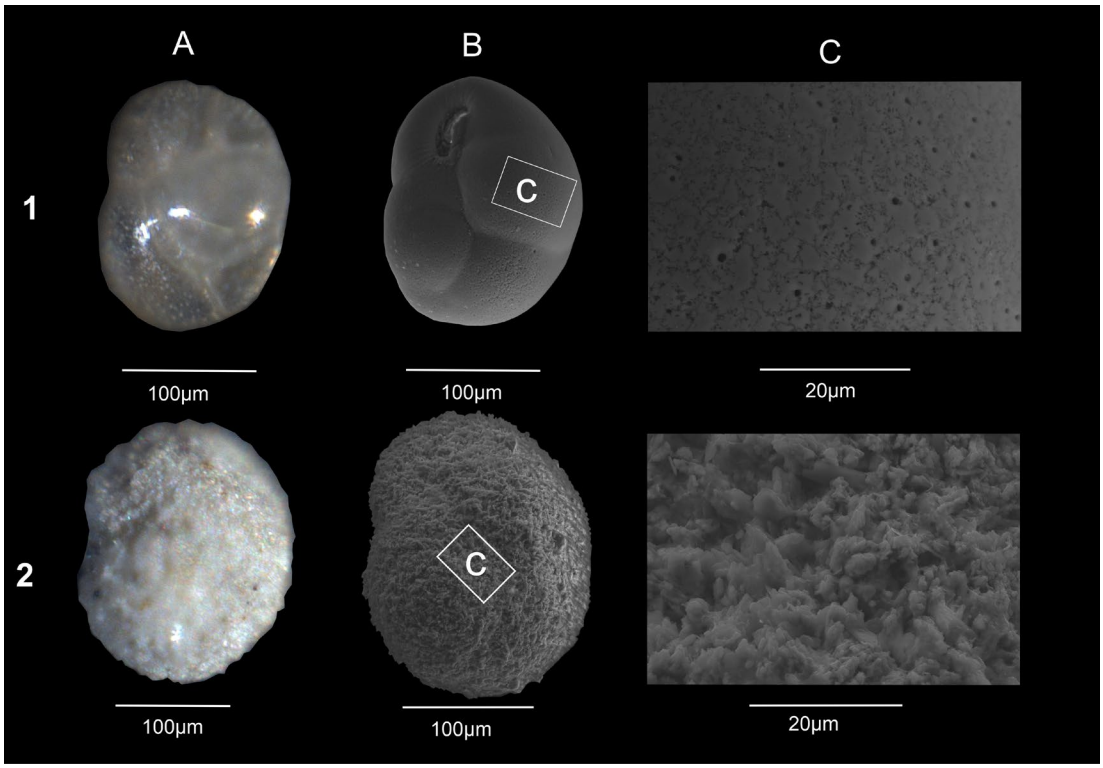

Figure 19. Row 1) *Pristine C. reniforme with $\delta^{13}C$ value of 1.87‰,* ***Row 2)*** *C. reniforme with major diagenetic alteration and with $\delta^{13}C$ value of -10.16‰.* ***Columns: A)*** *The view through stereomicroscope,* ***B)*** *SEM image of the exterior wall,* ***C)*** *zoomed SEM image.*

5. Discussion

Past methane releases from marine reservoirs have been linked to climate changes and an increase in the temperature during the Quaternary and the Paleocene (Wefer et al., 1994; Smith et al., 2001), Late Paleocene (Dickens et al., 1997), and Cretaceous (Jahren et al., 2001). Several studies used isotopic signature ($\delta^{13}C$) of planktic and benthic fossil foraminiferal tests to reconstruct past methane seepages (Millo et al., 2005; Consolaro et al., 2015; Sztybor and Rasmussen, 2017; Schneider et al., 2017).

Depleted foraminiferal $\delta^{13}C$ values can result from incorporating methane derived depleted $\delta^{13}C$ in various suggested ways during the biomineralization and as postmortem. During biomineralization benthic foraminifera can incorporate depleted ^{13}C from DIC species (carbon dioxide CO_2 and bicarbonate HCO_3^{2-}) from the ambient pore water and from intracellular storage of inorganic carbon (de Nooijer et al., 2009; Toyofuku et al., 2017). It has been also suggested that benthic foraminifera can incorporate low $\delta^{13}C$ via feeding on methanotrophic bacteria or having symbiosis with them (Melaniuk et al., 2022; Hill et al., 2003). Feeding on $\delta^{13}C$ depleted microbes has shown to be able to lower the $\delta^{13}C$ values down to -6‰ (Hill et al.,

2003). Empty foraminiferal tests can get passively coated by methane derived authigenic carbonates (MDAC) manifested by a high- Mg content and significantly lower $\delta^{13}C$ values (Schneider et al. 2017) (see chapter 2.3). Similar to this, in my study the SEM-EDS investigation of *C. neoteretis* with $\delta^{13}C$ value of -11.34‰ (at depth 286cm) revealed widespread MDAC precipitations, characterized by a high-Mg calcite crystals. The specimen was defined as having ´major diagenetic alteration that have started to form solid crust on top of the exterior wall (Fig. 17).

5.1 Core 1070 from the flank of the GHP5

Benthic and planktic $\delta^{13}C$ records combined with the visual investigation of the foraminiferal tests from the core 1070 revealed several past seepage events from the presently inactive GHP5. Significantly low benthic $\delta^{13}C$ values (from -5.99 to -11.34‰) indicative of the past seepage events were found between 190 – 290 cm from the deglaciation deposits (Fig. 20). The benthic foraminiferal species selected for the stable carbon isotope investigation was shallow infaunal species *Cassidulina neoteretis*. *Cassidulina neoteretis* has been previously shown to be capable of living within the hostile methane induced environment with low oxygen and high CO_2 concentrations, and possibly with the presence of hydrogen sulfide, as shown at the Håkon Mosby Mud Volcano (Wollenburg and Mackensen, 2009) and at Vestnesa Ridge (Melaniuk et al, 2022; Dessandier et al., 2019).

A previous study showed that *C. neoteretis* can incorporate depleted $\delta^{13}C$ if the seepage is only moderate but strong methane seepage will lead to their death (Melaniuk et al., 2022). Significantly depleted $\delta^{13}C$ values of -6 ‰ or lower are considered to be the result of postmortem precipitation of Methane Derived Authigenic Carbonates (MDAC) (Melaniuk, 2022, Schneider et a, 2017; Torres et al. 2003; Sztybor and Rasmussen, 2017). Additionally, MDAC coating is manifested by a high- Mg content (Schneider et al. 2017). Similar, in my study the SEM-EDS investigation of *C. neoteretis* with $\delta^{13}C$ value of -11.34‰ (at depth 286cm) revealed widespread MDAC precipitations, characterized by a high-Mg calcite crystals. The specimen was defined as having major diagenetic alteration that have started to form solid crust on top of the exterior wall (Fig. 17).

Significantly low planktic $\delta^{13}C$ values varied between -6.56 and -8.26‰ (Fig. 20). The planktic species selected to the isotopic measurements was *Neogloboquadrina pachyderma*. The expected normal $\delta^{13}C$ value for *N. pachyderma* in non- methane affected surface waters varies

from -0.5 to 0.5 ‰ (Zamelczyk et al., 2014; Werner et al., 2016). *Neogloboquadrina pachyderma* precipitate its test from the DIC species in the ambient surface waters, and thus reflects the environmental conditions within the water column (Torres et al. 2003). Therefore, the depleted $\delta^{13}C$ values of *N. pachyderma* in my study (from -6.56 to -8.26 ‰) are most likely resulted from postmortem secondary MDAC precipitation covering the test, making planktic foraminifera a good indicator for MDAC precipitations at methane charged sites (Schneider et al., 2017; Martin et al., 2010; Uchida et al., 2004; Torres et al., 2003). In the visual investigation, *N. pachyderma* with significantly depleted $\delta^{13}C$ value of -8.26‰ (at depth 286 cm) was defined as having ´major diagenetic alteration´. The SEM-EDS imagery revealed plugged pores and pervasive high-Mg calcite crystals that had started to form solid crust on the exterior wall (Fig. 18).

It has been suggested that the $\delta^{18}O$ rich digenetic fluids in the sediment could influence the $\delta^{18}O$ signature of the postmortem planktic and benthic foraminiferal $\delta^{18}O$ signature by increasing it up to ~5 - 7‰ (Dessandier et al. 2020; Cook et al. 2011). Nevertheless, the foraminiferal $\delta^{18}O$ record of the core 1070 do not support this hypothesis, because the planktic $\delta^{18}O$ values range between 2.52 – 3.65‰ (Fig. 20) and benthic $\delta^{18}O$ values vary between 2.35 – 4.66‰ reflecting the values similar to the values from non-seep areas (2.8 - 5.6‰) (Sztybor and Rasmussen 2017; Zamelczyk et al. 2014, 2012; Jessen et al., 2010; Rasmussen et al., 2007).

The solid phase element concentrations of the sediment were used to trace early diagenetic processes linked to biogeochemical cycling around the SMTZ. Several diagenetically interesting intervals were found from the Holocene sediments within the topmost ~50 cm and especially from the deglaciation (and possibly Early Holocene) deposits between 150 – 280 cm (Fig. 20).

Three distinct zones with barium enrichments were found around 25, 42 and 255 cm with values of 0.7, 1.3 and 0.8 respectively (Fig. 20). In addition, X-ray imagery revealed dark and dense precipitations scattered within these sediment layers (Fig. 9 and 20). It is possible that these enrichments represent barite fronts that are known to precipitate at or just above the SMTZ with sulphate depletion (Venneste et al., 2013; Greinert et al., 2002; Aloisi et al., 2004; Castellini et al., 2006). These fronts are formed when upward ascending dissolved barium precipitates with downward diffusing pore water sulphate as microcrystalline authigenic barite ($BaSO_4$). Authigenic barite ($BaSO_4$) has been considered as a proxy for the depth of modern and relict

SMTZs and past methane fluxes (Dickens, 2001) The Ba/Rb results correlate well with the earlier published Ba/Ti record by Yao et al., (2020).

Right below the barite front, a slight sulphur enrichment is found around 53 cm with value of 0.9 (Fig. 20) Several other sulphur enrichments are found further down from the deglaciation (and possibly Early Holocene) deposits between 150 – 280 cm with varying values between 0.9 and 1.5 (Fig. 20). Within these depths, the amount of barium is low indicating that the sulphur enrichments are not bounded in barite ($FaSO_4$). It can also be seen that the sulphur enrichments are accompanied with low magnetic susceptibility. Based on these observations the sulphur enrichments could imply the precipitation of authigenic Fe sulphides (Märtz et al., 2008). Of all formed Fe sulphides around the SMTZ, pyrite (FeS_2) is paramagnetic mineral and thus causing low magnetic susceptibility. On the other hand, the sulphur enrichments are not accompanied with Fe enrichment, making it challenging to interpret if the S enrichment actually indicates pyrite precipitation. However, authigenic Pyrite (FeS_2) is known to precipitate at the SMTZ (Berner, 1984; Canfield, 1989; Passier and Dekkers, 2002; Garming et al., 2005; Novosel et al., 2005; Riedinger et al., 2005). The solid phase barite front around 20-50 cm and the precipitation of pyrite below it could though indicate that the present day SMTZ is located right below 50 cm. Pyrite is known to precipitate at the SMTZ and barite above it. In addition, previously published pore water profiles by Gründger et al., 2019 and Hong et al., 2018 indicate that the modern SMTZ indeed locates just below 50 cm based on the sulphate and methane concentrations.

Solid phase enrichments of phosphorous (P), manganese (Mn) and iron (Fe) were found together from two distinct intervals from deglaciation deposits at 236 and 255 cm (Fig. 20). At 236 the values are 0.4 for phosphorous, 1.6 for manganese and 3.7 for iron. At 255 cm the values are 0.1 for phosphorous, 1.6 for manganese and 3.5 for iron (Fig. 20). The geochemical cycle of P and Fe are known to have a strong connection. A possible explanation for the enrichment of solid phase P, Fe and Mn at the same intervals could be the precipitation of authigenic phosphate mineral like Mn-rich vivianite ($Fe_3(PO_4)_2\ 8H_2O$). Sulphate methane transition zones (SMTZ) have been suggested to be biogeochemical hotspots of P cycling with Fe (II) phosphates precipitating below it in the methanic zone (März et al., 2018).

In addition, a piece of carbonate crust was found from top of the core (Fig. 9 and 20). Precipitation of carbonate crust on the sea floor indicates that the SMTZ has previously situated in the topmost sediments.

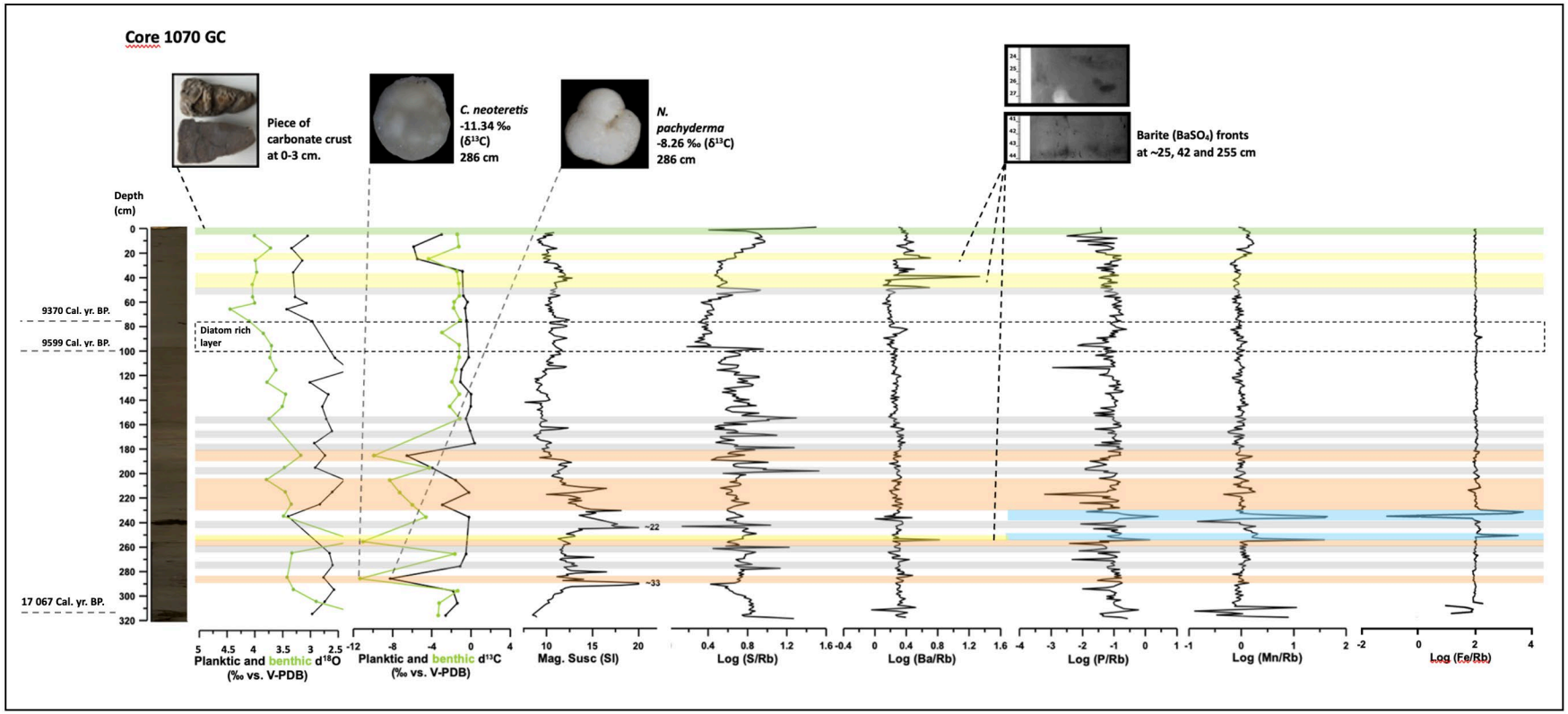

Figure 20. *Core 1070, combined proxy data for the past methane seepage events and early diagenetic processes.* ***From left:*** *the $\delta^{18}O$ and $\delta^{13}C$ signal of planktic N. pachyderma and benthic C. neoteretis, magnetic susceptibility, and the solid-phase elemental composition (S, Ba, P, Mn and Fe) of the sediment normalized against Rb.* ***Orange bars*** *indicate negative $\delta^{13}C$ excursions.* ***Yellow bars*** *indicate the depth of the barite front.* ***Grey bars*** *indicate pyrite precipitations.* ***Green bar*** *indicate the depth of piece of carbonate crust.*

5.2 1069 from the top of the GHP5

Benthic and planktic $\delta^{13}C$ records combined with the visual investigation of the foraminiferal tests from the core 1069 from the top of the post-active GHP5, revealed several past methane seepages. Several significantly depleted benthic and planktic $\delta^{13}C$ values were found from the Holocene sediments between 11 – 78 cm with benthic values varying between -4.78 and -10.16 ‰ and planktic between -1.29 and -5.81 ‰ (Fig. 21).

The benthic species selected for the isotopic measurements in the core 1069 was *Cassidulina reniforme.* In this study the normal marine $\delta^{13}C$ values for *C. reniforme* are expected to be similar to non-methane affected $\delta^{13}C$ values in *C. neoteretis* (0 to 1‰) (Wollenburg et al., 2001) The visual investigation of *C. reniforme* with $\delta^{13}C$ value of -10.16‰ (depth 11cm) revealed pervasive and thick coating of crystals covering the exterior wall indicating postmortem precipitation of Methane Derived Authigenic Carbonates (MDAC) (Melaniuk, 2022, Schneider et a, 2017; Torres et al. 2003; Sztybor and Rasmussen, 2017) (Fig. 19 and 21).

The planktic species selected to the stable isotope investigation for the core 1069 was *Neogloboquadrina pachyderma.* The expected normal $\delta^{13}C$ values for *N. pachyderma* in non-affected by methane surface water varies between -0.5 and 0.5 ‰ (Zamelczyk et al., 2014; Werner et al., 2016). Thus, the depleted $\delta^{13}C$ values within the topmost ~80 cm (Fig. 21) most likely represents the post-mortem secondary MDAC precipitation on the test. In the visual investigation *N. pachyderma* with $\delta^{13}C$ value of 0.14‰ (depth 116 cm) was defined as ´pristine´ according to the $\delta^{13}C$ value. In contrast to what was expected, the SEM-EDS imagery revealed plugged pores and high-Mg calcite crystals on the exterior wall (Fig. 18). The reason for this is unknown.

Planktic foraminifera were absent below 117 cm and benthic foraminifera below 144 cm (Fig. 21). The core 1069 was cored from the top of the GHP5 (Fig. 2b). In contrast to the core 1069, foraminifera were present throughout core 1070 that was cored from the flank of the GHP5 (Fig. 2b and 20). As the methane seepage is concentrated to the GHP summits (Serov et al., 2017), the absence of the foraminifera in the core 1069 could indicate an inhospitable living environment for the foraminifera during past methane seepage events. Indeed, an earlier study by Melaniuk (2021) from the active neighboring GHP1 showed that the distribution and density of modern benthic foraminifera was found to be zero on the top of the pingo and the highest at the edge of the pingo. It was suggested that the absence of the foraminifera on top of the pingo

was caused by sedimentary disturbance due to the passage of gas bubbles and low oxygen levels or the presence of hydrogen sulfide (Herguera et al., 2014; Carrier et al., 2020).

The solid phase element concentrations of the sediment were used to trace early diagenetic processes linked to biogeochemical cycling around the sulphate methane transition zone (SMTZ) (März et al., 2008). Two interesting intervals were found from the core 1069. The first one was found from Holocene deposits between 43 – 50 cm with barium enrichments with top wards decreasing values between 0.8 and 0.5 (Fig. 21). In addition, the x-ray images revealed dark and dense precipitation scattered within the sediment. This layer was interpreted as barite ($BaSO_4$) front (Fig. 21).

The second interval was found at ~160 cm (Fig. 21). The interval is characterized by enrichments of sulphur (S) and iron (Fe) with values of 2.0 and 2.1 respectively. In addition, lithological investigation revealed a block with a size of ~5.5 x 2.5 cm, rusty iron color and with mineral fragments with brass-yellow color and metallic luster between ~160 – 163 cm (Fig. 13 and 21) This interval was accompanied with low magnetic susceptibility with value of ~10.12 SI which is lower than the average value of the whole MS record (10.7 SI) (Fig. 21). Based on the combined observations of S and Fe enrichments, the low MS values indicating paramagnetic minerals and the properties of the large block, this layer is interpreted as containing pyrite (FeS_2).

Mn enrichment with a value of 0.6 is found at 151 cm is not accompanied with any other element enrichment, and it remains unclear what this could indicate (Fig. 21).

Neither the planktic nor benthic $\delta^{18}O$ record of the core 1069 do not support the hypothesis by Dessandier et al. (2020) and Cook et al. (2011) that the $\delta^{18}O$ rich digenetic fluids in the sediment could influence the postmortem foraminiferal $\delta^{18}O$ signature by increasing the $\delta^{18}O$ signature up to ~5 – 7 ‰. The planktic $\delta^{18}O$ values vary between 2.57 and 4.83 ‰ and the benthic $\delta^{18}O$ values vary between 4.42 and 4.82 ‰ reflecting the values similar to non-seep areas (2.8 - 5.6‰) (Sztybor and Rasmussen 2017; Zamelczyk et al. 2014, 2012; Jessen et al., 2010; Rasmussen et al., 2007) (Fig. 21).

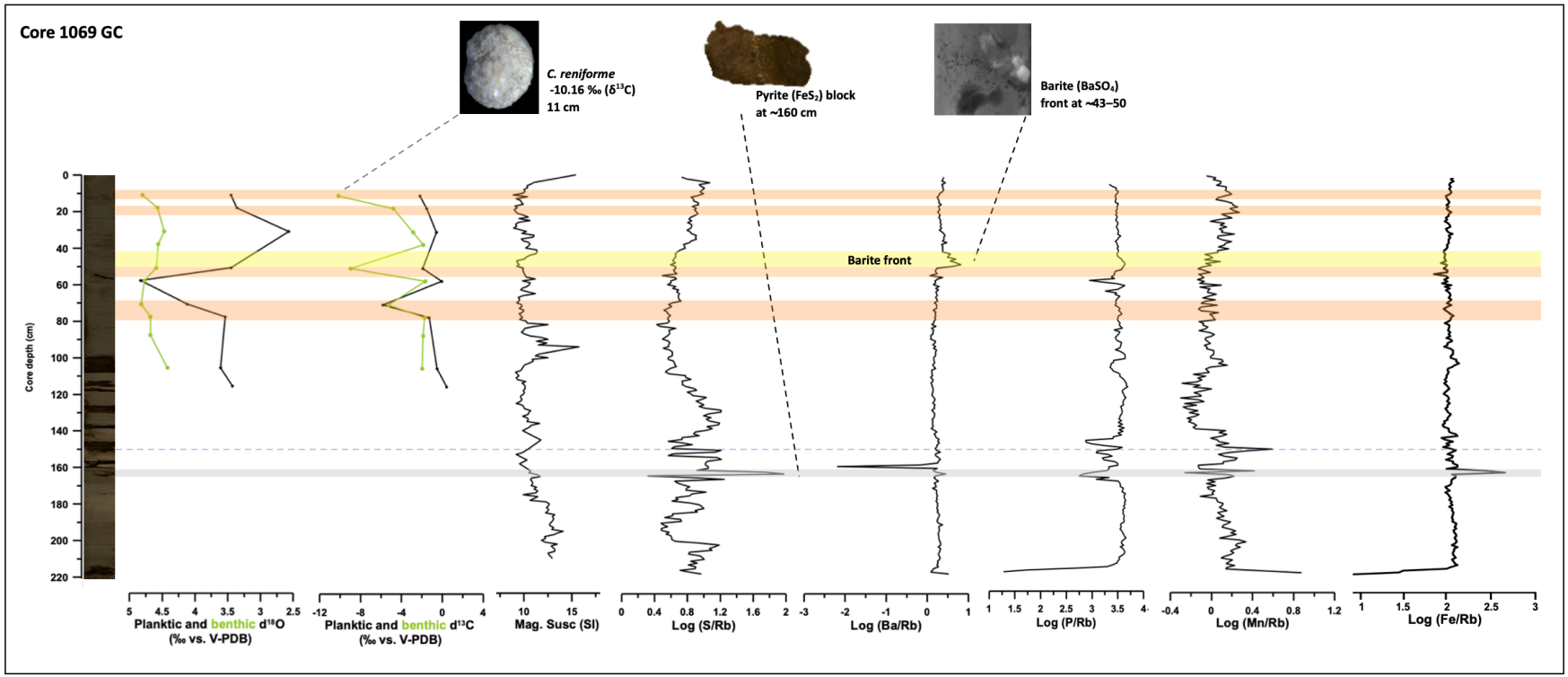

Figure 21. *Core 1069, combined proxy data for the past methane seepage events and early diagenetic processes. From left: the δ13C signal of planktic N. pachyderma and benthic C. reniforme, magnetic susceptibility, and the solid-state elemental composition (S, Ba, P, Mn, Fe) of the sediment normalized against Rb.* ***Orange bars*** *indicate negative excursion in the $\delta^{13}C$ signal.* ***Grey bar*** *indicates the depth of the pyrite layer.* ***Blue dashed line*** *indicate the depth of Mn enrichment.*

Summary and conclusions

Two gravity cores, the core 1070 from the flank of the GHP5 and the core 1069 from the top of the GHP5, were investigated to find possible relationship between isotopic signature of fossil foraminifera and past methane emission at Storfjordrenna Pingos site during the last deglaciation in context of past climatic changes.

The main objectives were to investigate the isotopic signatures ($\delta^{13}C$ and $\delta^{18}O$) of foraminiferal tests from sediments affected by methane, the microstructure and elemental distribution of the foraminiferal tests (SEM-EDS), and the solid-state chemical composition of the sediment (XRF).

Combined benthic and planktic $\delta^{13}C$ records, visual investigations (SEM-EDS) of the foraminiferal tests and the solid phase composition of the sediment (XRF) revealed interesting and complex methane seepage history at the presently inactive GHP5.

- **Foraminiferal $\delta^{13}C$ records** revealed distinct paleo seepage events from both cores. The oldest events are recorded in the core 1070 from the flank of the GHP5 corresponding to the deglaciation deposits (Fig. 22). The most recent events are found from the Holocene deposits from the core 1069 from the top of the GHP5 (Fig. 22).
- **The foraminiferal $\delta^{18}O$ record** from both cores did not support the hypothesis by Dessandier et al., (2020) and Cook et al., (2011) that the $\delta^{18}O$ rich digenetic fluids in the sediment could influence the $\delta^{18}O$ signature of the postmortem planktic and benthic foraminiferal $\delta^{18}O$ signature. Instead, the $\delta^{18}O$ signature reflected the values similar to values from non-seep areas (2.8 - 5.6‰) (Fig. 20 and 21) (Sztybor and Rasmussen 2017; Zamelczyk et al. 2014, 2012; Jessen et al., 2010; Rasmussen et al., 2007).
- **The visual investigation (SEM-EDS)** of foraminiferal tests from the intervals with significantly depleted $\delta^{13}C$ values revealed pervasive high-Mg calcite crystals that had started to form solid crust on the exterior wall plugging the pores, indicative of passive postmortem precipitation of MDAC. The specimens were defined as having ´major diagenetic alteration´ (Fig. 17, 18 and 19)
- **The solid phase composition of the sediment (XRF- analysis)** revealed precipitations of authigenic minerals accompanied with the distinct paleo seepage events recorded by the $\delta^{13}C$ records from both of the cores indicative of early diagenetic processes at the paleo Sulphate-Methane Transition Zones (SMTZs) (Fig. 20, 21 and 22) (Funk et al.

2004; März et al., 2008, 2018). Distinct Barite fronts were found from both cores from the Holocene deposits above 50 cm (Fig. 20, 21 and 22) indicative of modern SMTZ location below 50 cm. A piece of carbonate crust was found from the top of the core 1070 indicating the presence of the paleo SMTZ close to the sea floor (Fig. 20).

- Agglutinated foraminifera are mostly absent in both cores. Planktic foraminifera are mainly rare throughout both cores. Foraminifera were absent in 1069 (on the top of the GHP5) below 117 cm (planktic) and 144 cm (benthic). In the core 1070 (on the flank of the GHP5) they are present throughout the core. The absence might be related to the strong methane seepage in the past as described from GHP1 (Melaniuk et al., 2022)
- In both cores IRD is absent or very low within the Holocene sediments. Pre-Holocene sediments are characterized by alternating hemipelagic and glaciogenic deposits. Light brown layer with rather sharp boundaries is found from both cores at the same depth (1069: ~166 – 187 cm) (1070: ~165 – 188 cm). The color change indicates some kind of change in the sedimentation environment and sharp boundaries indicate rapid change. Laminated mud is found from 1069 (on the top of the GHP5) right below the light brown sediment at ~186 – 210 cm most likely representing the well-known distinct lithological shift in the sedimentological records of Storfjorden Trough and in the whole Barents Sea region (Svendsen et al., 1996; Aagaard-Sørensen et al., 2010; Jessen et al., 2010; Junttila et al., 2010; Nielsen and Rasmussen, 2018; Rasmussen and Thomsen, 2021). The relatively consistent ages obtained above and below the laminated interval have indicated that the layer has been deposited around 14,400 cal years BP corresponding to the Bølling interstadial (Jessen et al., 2010; Rasmussen and Thomsen, 2021). The laminated interval was not found from the core 1070 (Fig. 10 and 14)

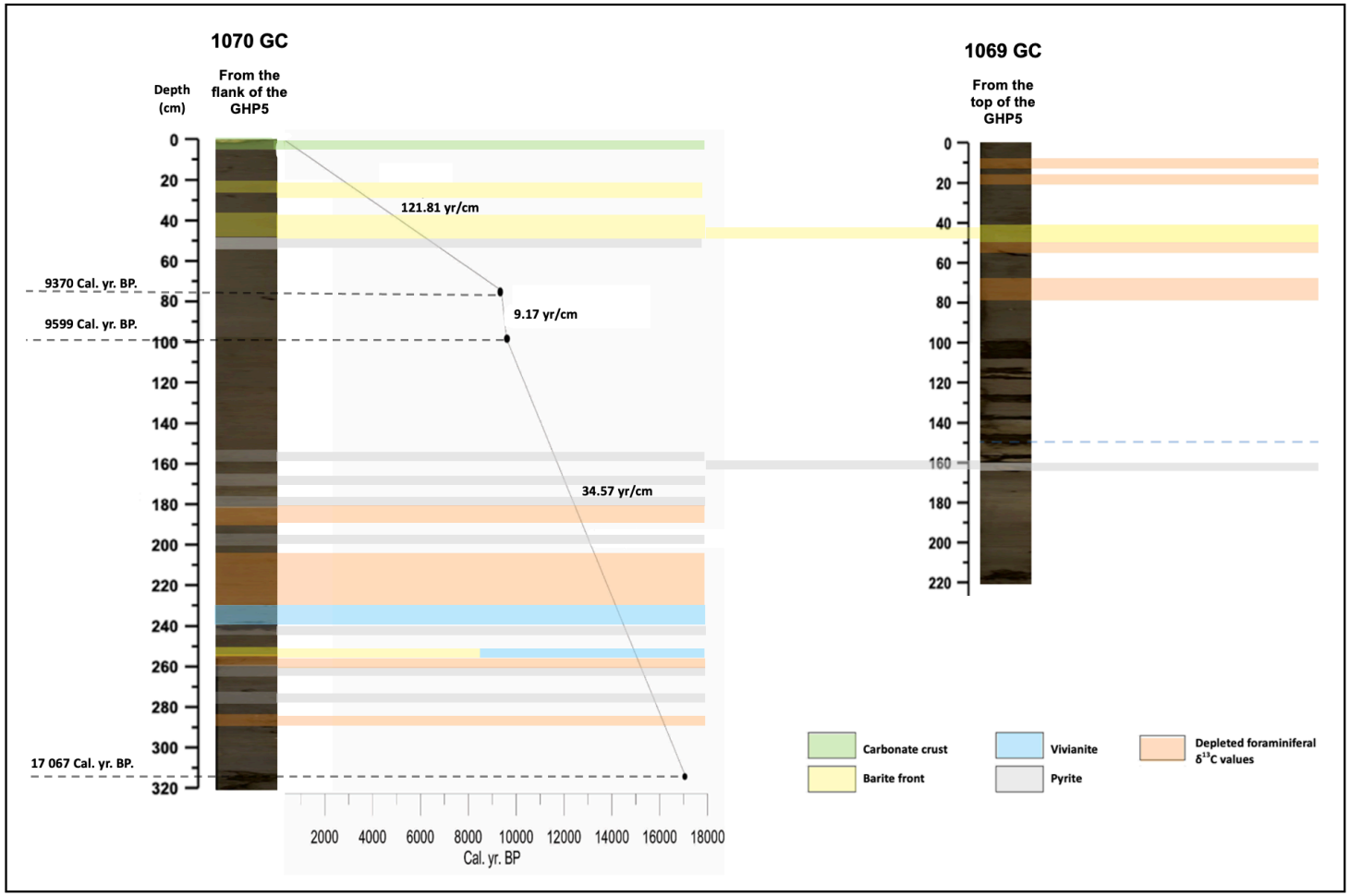

Figure 22. *Comparison of depleted $\delta^{13}C$ values and solid phase composition of the cores 1070 and 1069, accompanied with the age-depth model.*

Works cited

Aagaard-Sørensen, S., Husum, K., Knies, J., 2010. Paleoceanographic development in the SW Barents Sea during the Late Weichselian-Early Holocene transition. Quaternary Science Reviews 29, 3442-3456.

Aloisi, G. & Catherine, P. & Rouchy, J.-M., Foucher, J.-P. & Woodside, J. 2000. Methane-related authigenic carbonates of Eastern Mediterranean Sea mud volcanoes and their possible relation to gas hydrate destabilisation. Earth and Planetary Science Letters. 184. 321-338. 10.1016/S0012-821X(00)00322-8.

Alve, E. B. & Bernhard, J. M., 1995. Vertical migratory response of benthic foraminifera to controlled oxygen concentrations in an experimental microcosm. Marine Ecology Progress Series 116, 137–151.

Andrews J. T., Stein R., Moros M. & Perner K., 2016. Late Quaternary changes in sediment composition on the NE Greenland margin (~73° N) with a focus on the fjords and shelf. Boreas 45, 381–397, doi: 10.1111/bor.12169.

Armstrong, H. A. & Brasier, M., 2005. Microfossils. Blackwell Publishing, 296 p.

Arnold, A. J. & Parker, W. C., 1999. Biogeography of planktonic foraminifera, In: Sen Gupta, B.K. (Eds.) Modern Foraminifera. Kluwer Academic Publishers, Great Britain, pp. 103 – 122.

Asbjørnsen, H., Årthun, M., Skagseth, Ø. & Eldevik, T., 2020. Mechanisms underlying recent arctic atlantification. Geophysical Research Letters 47, e2020GL088036

Bé, A. W. 1977. An ecological, zoogeographic and taxonomic review of recent planktonic foraminifera.

Bé, A. H. W. & Tolderlund, D. S., 1971. Distribution and ecology of living planktonic foraminifera in surface waters of the Atlantic and Indian Oceans. In B.M. Funnell & W.R. Riedel (eds.): The micropaleontology of the oceans. Pp. 105–149. Cambridge: Cambridge University Press.

Bennett, M. R. & Glasser, N. F., 2009. Glacial Geology: Ice Sheets and Landforms. John Wiley & sons, Ltd, 375 p.

Bernhard, J. M., Martin, J. B. & Rathburn, A. E., 2010. Combined carbonate carbon isotopic and cellular ultrastructural studies of individual benthic foraminifera: 2. Toward an understanding of apparent disequilibrium in hydrocarbon seeps. *Paleoceanography* https://doi.org/10.1029/2010PA001930

Boetius, A., Ravenschlag, K., Schubert, C. J., Rickert, D., Widdel, F., Gieseke, A., Amann, R., Barker Jørgensen, B., Witte, U., & Pfannkuche, O. 2000. "A marine microbial consortium apparently mediating anaerobic oxidation of methane." *Nature* 407 (6804): 623-626. https://doi.org/10.1038/35036572.

Boltovskoy, E., Boltovskoy, D., Correa, N. & Brandini, F., 1996. Planktic foraminifera from the southwestern Atlantic (30°–60°S): species-specific patterns in the upper 50 m. Marine Micropaleontology 28, 53–72.

Bradley, R. S., 2015. Paleoclimatology: reconstructing climates of the Quaternary. Elsevier Inc, 675 p.

Consolaro, C., Rasmussen, T. L., Panieri, G., Mienert, J., Bünz, S., & Sztybor, K. 2015. Carbon isotope ($\delta^{13}C$) excursions suggest times of major methane release during the last 14 kyr in Fram Strait, the deep-water gateway to the Arctic, Clim. Past, 11, 669–685, https://doi.org/10.5194/cp-11-669-2015.

Cook, M. S., Keigwin, L. D., Birgel, D. & Hinrichs, K.-U., 2011. Repeated pulses of vertical methane flux recorded in glacial sediments from the southeast Bering Sea. *Paleoceanography*https://doi.org/10.1029/2010PA001993 (2011).

de Nooijer, L. J., Langer, G., Nehrke, G., & Bijma, J. (2009). Physiological controls on seawater uptake and calcification in the benthic foraminifer Ammonia tepida. Biogeosciences 6, 2669–2675. doi: 10.5194/bg-6-2669-2009

Dessandier, P., Borrelli, C., Yao, H., Sauer, S., Hong, W. L., & Panieri, G., 2020. Foraminiferal δ18 O reveals gas hydrate dissociation in Arctic and North Atlantic Ocean sediments. *Geo Mar. Lett.* 40, 507–523. doi: 10.1007/s00367- 019- 00635- 6

Dickens, G. R., Castillo, M. M. & Walker, J. C. G., 1997. "A blast of gas in the latest Paleocene: Simulating first-order effects of massive dissociation of oceanic methane hydrate." *Geology* 25 (3): 259-262. https://doi.org/10.1130/0091-7613(1997)025.

Faure, G., 1998. Principles and applications of geochemistry. Prentice-Hall, 600 p.

Forwick, M., 2013. How to use XRF core scanner data acquired with the Avaatech XRF core scanner at the Department of Geology, University of Tromsø.

Freitas, F. S., Arndt, S., Hendry, K. R., Faust, J. C., Tessin, A. C. & März, C., 2022. Benthic organic matter transformation drives pH and carbonate chemistry in Arctic marine sediments. Global Biogeochemical Cycles, 36, e2021GB007187. https://doi.org/10.1029/2021GB007187

Funk, J. A., Von Dobeneck, T., & Reitz, A., 2004. Integrated rock magnetic and geochemical quantification of redoxomorphic iron mineral diagenesis in Late Quaternary sediments from the equatorial Atlantic. In: Wefer, G., Mulitza, S. and Ratmeyer, V. (eds) The South Atlantic in the Late Ouaternary: Reconstruction of Material Budgets and Current Systems. Springer, Berlin, 237-260.

Grobe, H., 1987. A simple Method for the Determination of Ice-Rafted Debris in Sediment Cores. Polarforschung 57 (3): 123 – 126.

Gustafsson, M. & Nordberg, K., 2001. Living (stained) benthic foraminiferal response to primary production and hydrography in the deepest part of the Gullmar Fjord, Swedish west coast, with comparison to Höglund´s 1927 material. *Journal of Foraminiferal Research 31, 2-11.*

Gründger, F., Carrier, V., Svenning, M.M. et al., 2019. Methane-fuelled biofilms predominantly composed of methanotrophic ANME-1 in Arctic gas hydrate-related sediments. Sci Rep 9, 9725. https://doi.org/10.1038/s41598-019-46209-5

Haarpainter, J., Gascard, J. C. & Haugan, P. M., 2001. Ice production and brine formation in Storfjorden, Svalbard. Journal of Geophysical Research 106 C7, 14 001–14 013.

Hayes, J. D., Imbrie, J. & Shackleton, N. J., 1976. Variations in the Earth´s orbit: pacemaker of the ice ages. Science 194, 1121-1132.

Heaton, T. J., Köhler, P., Butzin, M., Bard, E., Reimer, R. W., Wen, A., Bronk Ramsey, C., Grootes, P. M., Hughen, K. A., Kromer, B., Reimer, P. J., Adkins, J., Burke, A., Cook, M. S., Olsen, J. & Skinner, L. C., 2020. Marine20-the marine radiocarbon age calibration curve (0-55,000 cal BP). Radiocarbon 62. doi: 10.1017/RDC.2020.68.

Hill, T. M., Kennett, J. P. & Spero, H. J., 2003. Foraminifera as indicators of methane-rich environments: A study of modern methane seeps in Santa Barbara Channel, California. Marine Micropaleontology, 49, 123–138. https://doi.org/10.1016/S0377-8398(03)00032-X

Hong, W.-L., Torres, M. E., Carroll, J., Crémière, A., Panieri, G., Yao, H. & Serov, P., 2017. Seepage from an arctic shallow marine gas hydrate reservoir is insensitive to momentary ocean warming. Nature Communications, 8, 15,745. https://doi.org/10.1038/ncomms15745

Hong, W.-L., Torres, M.E., Portnov, A., Waage, M., Haley, B., Lepland, A., 2018. Variations in Gas and Water Pulses at an Arctic Seep: Fluid Sources and Methane Transport. Geophysical Research Letters 45, 4153–4162 https://doi.org/10.1029/2018GL077309

Hovland, M., Judd, A. G. & Burke, R. A., 1993. The global flux of methane from shallow submarine sediments. Chemosphere Volume 26, Issues 1–4, January–February 1993, Pages 559-578

Hovland, M. & Svensen, H., 2006. Submarine pingoes: Indicators of shallow gas hydrates in a pockmark at Nyegga, Norwegian Sea. Marine Geology, 228 (14), 15–23.

Howarth, R. W., Santoro, R., Ingraffea, A., 2011. Methane and the greenhouse-gas footprint of natural gas from shale formations. Climatic Change. DOI 10.1007/s10584-011-0061-5

Howat, I. M., Box, J. E., Ahn, J., Herrington, A., McFadden, E. M., 2010. Seasonal variability in the dynamics of marine-terminating outlet glaciers in Greenland. J. Glaciol. 56, 601–613.

IPCC, 2007. Climate change 2007: the physical science basis. Summary for policymakers, intergovernmental panel on climate change. Fourth Assessment Report. IPCC Secretariat, Geneva, pp. 1–18.

IPCC, 2023. Summary for Policymakers. In: *Climate Change 2023: Synthesis Report.*A Report of the Intergovernmental Panel on Climate Change. Contribution of Working Groups I, II and III to the Sixth Assessment Report of the Intergovernmental Panel on Climate Change [Core Writing Team, H. Lee and J. Romero (eds.)]. IPCC, Geneva, Switzerland, (in press).

Jahren, A., Hope, N. C. A., Sarmiento, G., Guerrero, J. & Amundson, R. 2001. "Terrestrial record of methane hydrate dissociation in the Early Cretaceous." *Geology* 29 (2): 159-162.

Jernas, P., Klitgaard-Kristensen, D., Koç, N. & Tverberg, V., 2010. Response of Recent Benthic Foraminifera to Inflow of Atlantic Water; Evidence from Annual Sampling in a Glacial Fjord, Svalbard. http://www.forams2010.uni-bonn.de/sites/ sessions/pdf/abstracts_forams_2010.pdf

Jessen, S. P., & Rasmussen, T. L., 2019. Ice-rafting patterns on the western Svalbard slope 74–0 ka: Interplay between ice-sheet activity, climate and ocean circulation. Boreas, 48(1), 236–256. https://doi.org/10.1111/bor.12358

Jessen, S. P., Rasmussen, T. L., Nielsen, T. & Solheim, A., 2010. A new Late Weichselian and Holocene marine chronology for the western Svalbard slope 30,000–0 cal years BP. Quaternary Science Reviews 29, 1301–1312.

Jorissen, F. J., 1999. Benthic foraminiferal microhabitats below the sediment-water interface, In: Sen Gupta, B.K. (Eds.) Modern Foraminifera. Kluwer Academic Publishers, Great Britain, pp. 161 – 179.

Judd, A. G. & Hovland, M., 2007. Seabed Fluid Flow – The impact on Geology, Biology and the Marine Environment. Cambridge University Press, Cambridge.

Junttila, J., Aagaard-Sørensen, S., Husum, K. & Hald, M., 2010. Late Glacial-Holocene clay minerals elucidating glacial history in the SW Barents Sea. Marine Geology 276, 71–85.

Knittel, K., Lösekann, T., Boetius, A., Kort, R. & Amann, R., 2005. "Diversity and Distribution of Methanotrophic Archaea at Cold Seeps." *Applied and Environmental Microbiology* 71 (1): 467-479. https://journals.asm.org/doi/abs/10.1128/AEM.71.1.467-479.2005

Koch, S., Berndt, C., Bialas, J., Haeckel, M., Crutchley, G., Papenberg, C., Klaeschen, D., Greinert, J., **2015.** Gas-controlled seafloor doming. Geology 43 (7), 571–574. https://doi-org.mime.uit.no/10.1130/G36596.1

Kvenvolden, K. A., 1988. Methane hydrate – a major reservoir of car- bon in the shallow geosphere? Chemical Geology 71, 41–51.

Kvenvolden, K. A., 1993. Gas hydrates geological perspective and global change. *Rev. Geophys.* 31, 173–187. doi: 10.1029/93RG00268

Kwok, R., & Rothrock, D. A. 2009. Decline in Arctic sea ice thickness from submarine and ICES at records: 1958–2008, *Geophys. Res. Lett.*, 36, L15501, doi:10.1029/2009GL039035.

Laberg, J. S. & Vorren, T. O., 1996. The glacier-fed fan at the mouth of Storfjorden trough, western Barents Sea: a comparative study. Geologische Rundschau 85, 338–349.

Lisiecki, L. E. & Raymo, M. E., 2005. A Pliocene-Pleistocene stack of 57 globally distributed benthic δ18O records. Paleoceanography 20, PA1003, doi: 10.1029/2004PA001071

Loeblich, A. R. & Tappan, H., 1953. Studies of Arctic foraminifera. Smithsonian Miscellaneous Collections 12, 1 – 150.

Loeblich Jr., A. R. & Tappan, H., 1988. Foraminiferal General and Their Classification: Van Nostrand Reinhold Company, New Yourk, 2 Volumes, 970 p.

Loeng, H., 1991. Features of the physical oceanographic conditions of the Barents Sea. Polar Research, 10:1, 5-18. DOI: 10.3402/polar.v10i1.6723

Long, D., Lammers, S., Linke, P., 1998. Possible hydrate mounds within large sea-floor craters in the Barents Sea. Geol Soc Lond Spec Publ 137 (1), 3–237. https://doi-org.mime.uit.no/10.1144/GSL.SP.1998.137.01.1

Lowe, J. & Walker, M., 2015. Reconstructing Quaternary Environments (3rd ed). Routledge, 568 p. https://doi.org/10.4324/9781315797496

Lucchi, R. G., Camerlenghi, R. A. M., Colmenero-Hidalgo, E., Sierro, F. J., Sagnotti, L., Urgeles, R., Melis, R., Morigi, C., Bárcena, M.-A., Giorgetti, G., Villa, G., Persico, D., Flores, J.-A., Rigual-Hernández, A. S., Pedrosa, M. T., Macri, P. & Caburlotto, A., 2013. Postglacial sedimentary processes on the Storfjorden and Kveithola trough mouth fans: Significance of extreme glacimarine sedimentation. Global and Planetary Change 111, 309-326. https://doi.org/10.1016/j.gloplacha.2013.10.008.

Mackensen, A., Wollenburg, J. & Laetitia, L., 2006. "Low δ13C in tests of live epibenthic and endobenthic foraminifera at a site of active methane seepage." *Paleoceanography* 21 (2).https://agupubs.onlinelibrary.wiley.com/doi/abs/10.1029/2005PA001196.

Martin, R. A., Nesbitt, E. A. & Campbell, K. A., 2010: The effects of anaerobic methane oxidation on benthic foraminiferal assemblages and stable isotopes on the Hikurangi Margin of eastern New Zealand. Marine Geology 272, 270–284.

Martinson, D. G., Pisias, N. G., Hays, J. D., Imbrie, J., Moore, T. C., Shackleton, N. J. 1987. Age dating and the orbital theory of the ice ages: development of a high-resolution 0 to 300,000-year chronostratigraphy. Quaternary Research 27 (1), 1–29. https://doi.org/10.1016/0033-5894(87)90046-9

Maslin, M., Owen, M., Betts, R., Day, S., Dunkley Jones, T. & Ridgwell, A., 2010. "Gas hydrates: past and future geohazard?" Philosophical Transactions of the Royal Society A, Mathematical, Physical and Engineering Sciences 368 (1919), 2369-93. https://doi.org/10.1098/rsta.2010.0065.

McCorkle, D. C., Keigwin, L. D., Corliss, B. H., & Emerson, S. R., 1990. The influence of microhabitats on the carbon isotopic composition of deep-sea benthic foraminifera. Paleoceanography 5, 161–185. doi: 10.1029/ PA005i002p00161

Melaniuk, K., Sztybor, K., Treude, T., Sommer, S. & Rasmussen T.L., 2022. Influence of methane seepage on isotopic signatures in living deep-sea benthic foraminifera, 79°N. Scientific Reports. 12:1169. https://doi.org/10.1038/s41598-022-05175-1

Midttun, L., 1985. Formation of dense bottom water in the Barents Sea. Deep-Sea Research 32, 1233–1241.

Millo, C., Sarnthein, M., Erlenkeuser, H., & Frederichs, T. (2005). Methane- driven late Pleistocene δ13C minima and overflow reversals in the southwestern Greenland Sea. Geology 33, 873–876. doi: 10.1130/G21790.1

Murray, J.W., 2006. Ecology and Applications of Benthic Foraminifera. Cambridge University Press, Cambridge.

März, C., Riedinger, N., Sena, C. & Kasten S., 2018. Phosphorus dynamics around the sulphate-methane transition in continental margin sediments: Authigenic apatite and Fe (II) phosphates. Elsevier, Marine geology, 404, 84 – 96. https://doi.org/10.1016/j.margeo.2018.07.010

März, C., Hoffmann, J., Bleil, U., de Lange, G. J. & Kasten, S., 2008. Diagenetic changes of magnetic and geochemical signals by anaerobic methane oxidation in sediments of the Zambesi deep-sea fan (SW Indian Ocean), Marine Geology, 255, pp. 118-130. doi: 10.1016/j.margeo.2008.05.013

März, C., Stratmann, A., Matthiessen, J., Meinhardt, A. K., Eckert, S., Schnetger, B., Vogt, C., Stein, R. & Brumsack, H. J., 2011. Manganese-rich brown layers in Arctic Ocean sediments: Composition, formation mechanisms, and diagenetic overprint. Geochimica et Cosmochimica Acta, 75(23). 7668-7687. doi:10.1016/j.gca.2011.09.046

Naehr, T. H., Eichhubl, P., Orphan, V. J., Hovland, M., Paull, C. K., Ussler, W., Lorenson, T. D. & Greene, H. G., 2007. Authigenic carbonate formation at hydrocarbon seeps in continental margin sediments: A comparative study. Deep. Res. Part II Top. Stud. Oceanogr. 54, 1268–1291. http://dx.doi.org/10.1016/j.dsr2.2007.04.010.

Nielsen, T. & Rasmussen, T. L., 2018. Reconstruction of ice sheet retreat after the Last Glacial maximum in Storfjorden, southern Svalbard. Marine Geology 402, 228–243.

Nørvang, A., 1945. The Zoology of Iceland, Foraminifera. *Copenhagen & Reykjavik: Ejnar Munksgaard.* v. 2, Part 2: 1-79. page(s): p. 41, text-figs. 6e—6h

Orphan, V. J., House, C. H., Hinrichs, K.-U., McKeegan, K. D. & DeLong, E. F., 2001. "Methane-Consuming Archaea Revealed by Directly Coupled Isotopic and Phylogenetic Analysis." *Science* 293 (5529): 484-487. https://doi.org/10.1126/science.1061338.

Orphan, V. J., Ussler, W. III, Naehr, T. H., House, C. H., Hinrichs, K.-U. & Paull, C. K., 2004: Geological, geochemical, and microbi- ological heterogeneity of the seafloor around methane vents in the Eel River Basin, offshore California. Chemical Geology 205, 265– 289.

Paull. C. & W. Dillon. 2001. Natural Gas Hydrates, Occurrence, Distribution, and Detection. American Geophysical Union Washington, DC. Geophysical Monograph Series 124, 315p.

Pearson, P. N., 2012. Oxygen isotopes in foraminifera: overview and historical review. The Paleontological Society Papers, vol. 18, 1-38.

Pedrosa, M. T., Camerlenghi, A., De Mol, B., Urgeles, R., Rebesco, M., Lucchi, R.G., and shipboard participants of the SVAIS and EGLACOM Cruiseset al., 2011. Seabed morphology and shallow sedimentary structure of the Storfjorden and Kveithola trough-mouth fans (North West Barents Sea). Marine Geology 286, 65–81.

Phrampus, B. J., & Hornbach, M. J., 2012. "Recent changes to the Gulf Stream causing widespread gas hydrate destabilization." *Nature* 490 (7421): 527-530. https://doi.org/10.1038/nature11528.

Piper, D. J. W., & Brisco, C. D., 1975. Deep-water continental-margin sedimentation. DSDP leg 28, Antarctica. - In: Hayes, D. E. & L. A. Frakes et al., eds. Initial Reports of the Deep Sea Drilling Project 28: 727-755. Washington.

Polyak, L., Best, K. M., Crawford, K. A., Council, E. A. & St-Onge, G., 2013. Quaternary history of sea ice in the western Arctic Ocean based on foraminifera. Quaternary Science Reviews 79, 145-156.

Polyakov, I. V., Pnyushkov, A. V., Alkire, M. B., Ashik, I. M., Baumann, T. M., Carmack, E. C., Goszczko, I., Gutherie, J., Ivanov, V. V., Kanzow, T., Krishfield, R., Kwok, R., Sundfjord, A., Morison, J., Rember, R. & Yulin, A., 2017. Greater role for Atlantic inflows on sea-ice loss in the Eurasian Basin of the Arctic Ocean. Science, 356(6335), 285–291. https://doi.org/10.1126/science.aai8204

Portnov, A., Vadakkepuliyambatta, S., Mienert, J. & Hubbard., A., 2016. Ice-sheet-driven methane storage and release in the Arctic. Nature communications, 7, 10314.

Rasmussen, S. O., Bigler, M., Blockley, S. P., Blunier, T., Buchardt, S. L., Clausen, H. B., Cvijanovic, I., Dahl-Jensen, D., Johnsen, S. J., Fischer, H., Gkinis, V., Guillevic, M., Hoek, W. Z., Lowe, J. J., Pedro, J. B., Popp, T., Seierstad, I. K., Steffensen, J. P., Svensson, A. M., Vallelonga, P., Vinther, B. M., Walker, M. J. C., Wheatley, J. J. & Winstrup, M., 2014a. A stratigraphic framework for abrupt climatic changes during the Last Glacial period based on three synchronized Greenland ice-core records: Refining and extending the INTIMATE event stratigraphy. Quaternary Science Reviews, 106, 14–28. https://doi.org/10.1016/j.quascirev.2014.09.007

Rasmussen, T. L., Thomsen, E., Skirbekk, K., Ślubowska-Woldengen, M., Klitgaard Kristensen, D. & Koç, N., 2014 a. Spatial and temporal distribution of Holocene temperature maxima in the northern Nordic seas: interplay of Atlantic-, Arctic- and polar water masses. Quaternary Science Reviews 92, 280–291.

Rasmussen, T. L. &Thomsen, E., 2014 b. Brine formation in relation to climate changes and ice retreat during the last 15,000 years in Storfjorden, Svalbard, 76–78°N. Paleoceanography, 29, 911–929, doi:10.1002/2014PA002643.

Rasmussen, T. L. & Thomsen, E., 2014 c. Palaeoceanographic development in Storfjorden, Svalbard, during the deglaciation and Holocene: evidence from benthic foraminiferal records. Boreas. 10.1111/bor.12098. ISSN 0300- 9483.

Rasmussen, T. L., Thomsen, E., Ślubowska, M. A., Jessen, S., Solheim, A. & Koç, N., 2007. Paleoceanographic evolution of the SW Svalbard margin (76°N) since 20,000 14C yr BP. Quaternary Research 67, 100–114.

Rasmussen, T. L. & Thomsen, E., 2021. Climate and ocean forcing of ice-sheet dynamics along the Svalbard-Barents Sea ice sheet during the deglaciation ~20,000–10,000 years BP. Quaternary Science Advances 3, 100019.

Rasmussen, T. L. & Thomsen, E., 2017. Ecology of deep-sea benthic foraminifera in the North Atlantic during the last glaciation: Food or temperature control. Palaeogeography, Palaeoclimatology, Palaeoecology, 472, 15–32. https://doi.org/10.1016/j.palaeo.2017.02.012

Rathburn, A. E., Levin, L. A., Held, Z. & Lohmann, K. C., 2000. Benthic foraminifera associated with cold methane seeps on the northern California margin: Ecology and stable

isotopic composition. Marine Micropaleontology. 38, 247–266. https://doi.org/10.1016/S0377- 8398(00)00005-0

Rathburn, A. E., Pérez, M. E., Martin, J. B., Day, S. A., Mahn, C., Gieskes, J., Ziebis, W., Williams, D. & Bahls, A., 2003. Relationships between the distribution and stable isotopic composition of living benthic foraminifera and cold methane seep biogeochemistry in Monterey Bay, California. Geochem. Geophys. Geosyst. 4:1106. doi:10.1029/2003GC000595

Ravelo, A. H. & Hillaire-Marcel, C., 2007. The use of oxygen and carbon isotopes of foraminifera in paleoceanography. In: Hillaire-Marcel, C., de Vernal, A. (Eds.), Proxies in Late Cenozoic Paleoceanography. Developments in Marine Geology 1, 735-764, Elsevier B.V

Reimer, P., Austin, W. E. N., Bard, E., Bayliss, A., Blackwell, P. G., Bronk Ramsey, C., Butzin, M., Cheng, H., Edwards, R. L., Friedrich, M., Grootes, P. M., Guilderson, T. P., Hajdas, I., Heaton, T. J., Hogg, A. G., Hughen, K. A., Kromer, B., Manning, S. W., Muscheler, R., Palmer, J. G., Pearson, C., van der Plicht, J., Reimer, R. W., Richards, D. A., Scott, E. M., Southon, J. R., Turney, C. S. M., Wacker, L., Adolphi, F., Büntgen, U., Capano, M., Fahrni, S. M., Fogtmann-Schulz, A., Friedrich, R., Köhler, P., Kudsk, S., Miyake, F., Olsen, J., Reinig, F., Sakamoto, M., Sookedo, A. & Talamo, S., 2020. The IntCal20 Northern Hemisphere Radiocarbon Age Calibration Curve (0–55 cal kBP). *Radiocarbon, 62*(4), 725-757. doi:10.1017/RDC.2020.41

Reimer, P. J., Bard, E., Bayliss, A., Beck, J. W., Blackwell, P. P., Ramsey, C. B., Buck, C. E., Cheng, H., Edwards, R. L., Friedrich, M., Grootes, P. M., Guilderson, T. P., Haflidason, H., Hajdas, I., Hatté, C., Heaton, T. J., Hoffmann, D. L., Hogg, A. G., Hughen, K. A., Kaiser, K. F., Kromer, B., Manning, S. W., Niu, M., Reimer, R. W., Richards, D. A., Scott, E. M., Southon, J. R., Staff, R. A., Turney, C. S. M. & van der Plicht, J., 2013. IntCal13 and Marine13 radiocarbon age calibration curves, 0–50,000 years cal BP. Radiocarbon 55, 1869–1887, doi: 10.2458/azu_js_rc.55.16947.

Romanek, C. S., Grossman, E. L. & Morse, J. W., 1992. Carbon isotopic fractionation in synthetic aragonite and calcite: Effects of temperature and precipitation rate. Geochimica et Cosmochimica Acta, 56 (1), 419-430. https://doi-org.mime.uit.no/10.1016/0016-7037(92)90142-6

Ruppel, C. D., & Kessler, J. D., 2017. The interaction of climate change and methane hydrates, *Rev. Geophys.*, 55, 126- 168, doi:10.1002/2016RG000534.

Schneider, A., Crémière, A., Panieri, G., Lepland, A. & Knies, J., 2017. Diagenetic alteration of benthic foraminifera from a methane seep site on Vestnesa Ridge (NW Svalbard). Deep Sea Research Part I: Oceanographic Research Papers, Volume 123, 22-34. https://doi.org/10.1016/j.dsr.2017.03. 001

Seidenkrantz, M.-S., 1995. Cassidulina teretis Tappan and Cassidulina neoteretis new species (Foraminifera): stratigraphic markers for deep sea and outer shelf areas. Journal of Micropalaeontology 14, 145–157.

Seidenkrantz, M.-S., 2013. Benthic foraminifera as palaeo sea-ice indicators in the subarctic realm - examples from the Labrador Sea-Baffin Bay region. Quaternary Science Reviews 79, 135-144.

Sen, A., Åström, E. K. L., Hong, W.-L., Portnov, A., Waage, M., Serov, P., Carroll, M.L. & Carroll, J., 2018. Geophysical and geochemical controls on the megafaunal community of a high Arctic cold seep. Biogeosciences 15, 4533–4559. https://doi.org/10.5194/bg-15-4533-2018

Serov, P., Vadakkepuliyambatta, S., Mienert, J., Patton, H., Portnov, A., Silyakova, A., Panieri, G., Carroll, M. L., Carroll, J., Andreassen, K. & Hubbard, A., 2017. Postglacial response of Arctic Ocean gas hydrates to climatic. PNAS 114, no. 24, 6215–6220.

Sexton, P. F., Wilson, P. A. & Pearson, P.N., 2006. Microstructural and geochemical perspectives on planktic foraminiferal preservation: "glassy" versus "frosty.". Geochemistry, Geophysics, Geosystems 7. http://dx.doi.org/10.1029/2006GC001291.

Shackleton, C. S., Winsborrow, M. C. M., Andreassen, K., Lucchi, R. G. & Bjarnadottir, L.R., 2020. Ice-margin retreat and grounding-zone dynamics during initial deglaciation of the Storfjordrenna Ice Stream, western Barents Sea. Boreas 49, 38–51.

Shakhova, N., Semiletov, I., Panteleev, G., 2005. The distribution of methane on the Siberian Arctic shelves: Implications for the marine methane cycle, Geophysical Research Letters 32

Shakhova, N., Semiletov, I., Leifer, I., Sergienko, V., Salyuk, A., Kosmach, D., Chernykh, D., Stubbs, C., Nicolsky, D., Tumskoy, V., Gustafsson, Ö., 2014. Ebullition and storm-induced methane release from the East Siberian Arctic Shelf. *Nature Geoscience* 7.1, 64-70. https://doi-org.mime.uit.no/10.1038/ngeo2007

Smith, L. M., Sachs, J. P., Jennings, A. E., Anderson, D. M. & deVernal, A., 2001. "Light δ13C events during deglaciation of the East Greenland Continental Shelf attributed to methane release from gas hydrates." *Geophysical Research Letters* 28 (11): 2217-2220. https://agupubs.onlinelibrary.wiley.com/doi/abs/10.1029/2000GL012627.

L09601, doi:10.1029/2005GL022751.

Sloan, E. D. D., 1990. Clathrate Hydrates of Natural Gases. New York: Marcel Dekker.

Spielhagen, R. F., Werner, K., Sørensen, S. A., Zamelczyk, K., Kandiano, E., Budeus, G., Husum, K., Marchitto, T. M. & Hald, M., 2011. Enhanced Modern Heat Transfer to the Arctic by Warm Atlantic Water. *Science,* **331**,450-453.DOI:10.1126/science.1197397

Stabell, B., 1986. A diatom maximum horizon in upper quaternary deposits. Geologische Rundschau (1910. Print) [Preprint]. https://doi.org/10.1007/bf01770186.

Steinsund, P. I., 1994. Benthic foraminifera in surface sediments of the Barents and Kara seas: modern and late Quaternary applications. Ph.D. thesis, University of Tromsø, 111 pp.

Stoner, J. S., Channell, J. E. T. & Hillaire-Marcel, C., 1996. The magnetic signature of rapidly deposited detrital layers from the deep Labrador Sea: relationship to North Atlantic Heinrich Layers. *Paleoceanography*, **11**: 309–325.

Strąpoć, D., Jacquet, B., Torres, O., Khan, S., Villegas, E. I., Albrecht, H., Okoh, B. & McKinney, D., 2020. "Deep biogenic methane and drilling-associated gas artifacts: Influence on gas-based characterization of petroleum fluids."A*APG Bulletin* 104 (4): 887-912.. https://doi.org/10.1306/08301918011.

Stuiver, M., Reimer, P. J., and Reimer, R. W.: CALIB 8.20 [WWW program], available at: http://calib.org, last access: 15 July 2021.

Stuiver, M. & Polach, H., 1977. Discussion-Reporting of 14. C data Radiocarbon. 19. 355-363. 10.1017/S0033822200003672.

Stuiver, M., & Reimer, P. J., 1993, Radiocarbon, 35, 215-230. CALIB rev. 8.2 Accessed 2022.

Sztybor, K. & Rasmussen, T. L., 2017. Diagenetic disturbances of marine sedimentary records from methane-influenced environments in the Fram Strait as indications of variation in seep intensity during the last 35 000 years. Boreas 46, 212 – 228. https://doi.org/10.1111/bor.12202

Torres, M. E., Mix, A. C., Kinports, K., Haley, B., Klinkhammer, G. P., McManus, J. & de Angelis, M. A., 2003. "Is methane venting at the seafloor recorded by δ13C of benthic foraminifera shells?" *Paleoceanography* 18 (3).

Toyofuku, T., Matsuo, M. Y., de Nooijer, L. J., Nagai, Y., Kawada, S., Fujita, K., Reichart, G.-J., Nomadi, H., Tsuchiya, M., Sakaguchi, H., Kitazato, H., Stratigraphy and paleontology. 2017. Proton pumping accompanies calcification in foraminifera. Nat. Commun. 8, 1–6. doi: 10.1038/ncomms14145

Uchida, M., Shibata, Y., Ohkushi, K., Ahagon, N. & Hoshiba, M. 2004: Episodic methane release events from Last Glacial marginal sediments in the western North Pacific. Geochemistry, Geophysics, Geosystems 5, Q08005, doi:10.1029/2004GC000699.

Vinje T. E., 1977. Sea ice conditions in the European sector of the marginal seas of the Arctic, 1966–75. Norsk Polarinstitutt Årbok. 1975, 163–174.

Vogt., >C.

Vorren, T. O. & Laberg, J. S., 1996. Late glacial air temperature, oceanography and ice sheet interactions in the southern Barents Sea region. In: Andrews, J.T., Austin, W.E.N., Bergsten, H., J.A.E. (Eds.), Late Quaternary Palaeoceanography of the North Atlantic Margins. Geological Society Special Publication. Geological Society of London, London, pp. 303–321.

Vorren, T. O., Richardsen, G., Knutsen, S. M. & Henriksen, E., 1991. Cenozoic erosion and sedimentation in the western Barents Sea. Marine and Petroleum Geology, 8(3), 317–340. https://doi.org/10.1016/0264-8172(91)90086-G

Waage, M., Portnov, A. D., Serov, P., Bünz, S., Waghorn, K. A., Vadakkepuliyambatta, S., Mienert, J. & Andreassen, K., 2019. Geological controls on fluid flow and gas hydrate pingo development on the Barents Sea margin. Geochemistry Geophysics Geosystems. https://doi.org/10.1029/2018GC007930.

Wefer, G., Heinze, P. M. & Berger, W. H., 1994. "Clues to ancient methane release." *Nature* 369 (6478): 282-282. https://doi.org/10.1038/369282a0.

Weltje, G. J. & Tjallingii, W., 2008. Calibration of XRF core scanners for quantitative geochemical logging of sediment cores: Theory and application. Earth and Planetary Science Letters 274, 423–438.

Wentworth, C. K., 1922. A scale of grade and class terms for clastic sediments. The Journal of Geology, 30(5), 377-392.

Werner, K., Müller, J., Husum, K., Spielhagen, R. F., Kandiano, E. S. & Polyak L., 2016. Holocene sea subsurface and surface water masses in the Fram Strait—comparisons of temperature and sea-ice reconstructions. Quaternary Science Reviews 147, 194–209. https://doi.org/10.1016/j.quascirev.2015.09.007

Whiticar, M. J., 1999. "Carbon and hydrogen isotope systematics of bacterial formation and oxidation of methane." *Chemical Geology* 161 (1): 291-314. https://www.sciencedirect.com/science/article/pii/S0009254199000923.

Wollenburg, J. E., Kuhnt, W. & Mackensen, A., 2001. Changes in Arctic Ocean paleoproductivity and hydrography during the last 145 kyr: the benthic foraminiferal record. ecovers-uppermost-1-2-meters Paleoceanography 16, 65–77.

Wollenburg, J. & Mackensen, A., 2009. The ecology and distribution of benthic foraminifera at the Håkon Mosby mud volcano (SW Barents Sea slope) , Deep-Sea Research I, 56 (8), pp. 1336-1370 . doi: 10.1016/j.dsr.2009.02.004

Wollenburg, J. E., Raitzsch, M. & Tiedemann, R., 2015. Novel high-pressure culture experiments on deep-sea benthic foraminifera— Evidence for methane seepage-related δ13C of Cibicides wuellerstorfi. Marine Micropaleontology. 117, 47–64. https://doi.org/10.1016/j.marmicro.2015.04.003

Yao, H., Niemann, H. & Panieri, G., 2020. Multi-proxy approach to unravel methane emission history of an Arctic cold seep. Quaternary Science Reviews 244. https://doi.org/10.1016/j.quascirev.2020.106490

Zamelczyk K., Rasmussen T. L., Raitzsch M. & Chierici M., 2020. The last two millennia: climate, ocean circulation and palaeoproductivity inferred from planktic foraminifera, south-western Svalbard margin. Polar Research, 39. https://doi.org/10.33265/polar.v39.3715

Zamelczyk, K., Rasmussen, T. L., Husum, K., Godtliebsen, F. & Hald, M., 2014. Surface water conditions and calcium carbonate preservation in the Fram Strait during marine isotope stage 2, 28.8–15.4 kyr. Paleoceanography 29, 1–12, doi:10.1002/2012PA 002448.

Zeebe, R. E., Bijma, J. & Wolf-Gladrow, D. A., 1999. A diffusion-reaction model of carbon isotope fractionation in foraminifera. Marine Chemistry, 64, 199–227.

Årthun, M., Eldevik, T., Smedsrud, L. H., Skagseth, O. & Ingvaldsen, R. B., 2012. Quantifying the influence of Atlantic heat on Barents Sea ice variability and retreat. Journal of Climate, 25(13), 4736–4743. https://doi.org/10.1175/JCLI-D-11-00466.1

Cronin, T., 2013, September 01, Gravity Corer Recovers the Uppermost 1-2 Meters of Sediment, USGS- Science For a Changing World. https://www.usgs.gov/media/images/gravity-corer-recovers-uppermost-1-2-meters-sediment

(01.01.22)

Appendix

Core 1069, #2. Upper row: working half. Lower row: archive half.

Figure 23. *Photos of the core 1069, #2.* ***Upper row:*** *working half,* ***Lower row:*** *archive half.*

Solid state element counts (XRF) of the cores 1070 and 1069

The XRF analysis was done with the Avaatech XRF core scanner. Pre-defined measuring time was set to 10 seconds. Based on the atomic number of the element, voltage of 10, 30 or 50 kV was used. The current was 1000 µA. No filter was used. The measurements were carried out with 10 mm interval and reported as counts per second (cps).

10 kv voltage was used for the following elements: Aluminium (Al), Silicon (Si), Phosphorus (P), Sulfur (S), Chlorine (Cl), Potassium (K), Calcium (Ca), Titanium (Ti), Chromium (Cr), Manganese (Mn), Iron (Fe), Rhodium (Rh).

30 kv voltage was used for the following elements: Copper (Cu), Zink (Zn), Gallium (Ga), Arsenic (As), Bromine (Br), Rubidium (Rb), Strontium (Sr), Zirconium (Zr), Niobium (Nb), Molybden (Mo), Lead (Pb).

50 kv voltage was used for the following elements: Silver (Ag), Tin (Sn), Iodine (I), Barium (Ba).

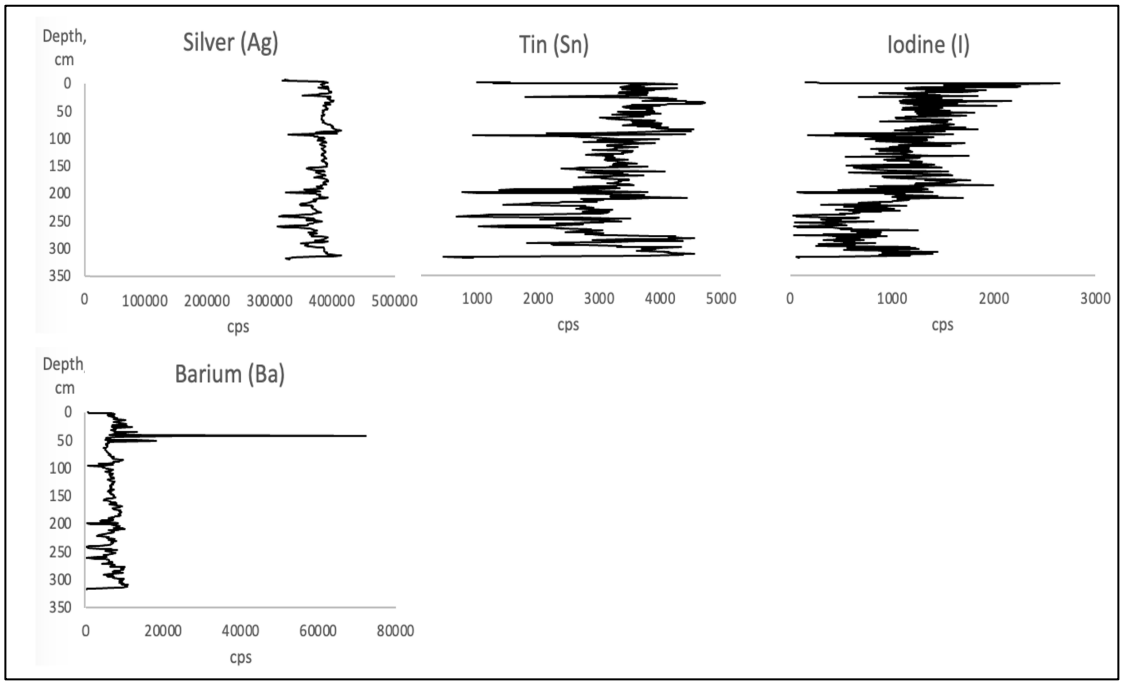

Figure 24. *Core 1070, solid phase element counts of Ag, Sn, I, Ba. Used voltage: 50 kv.*

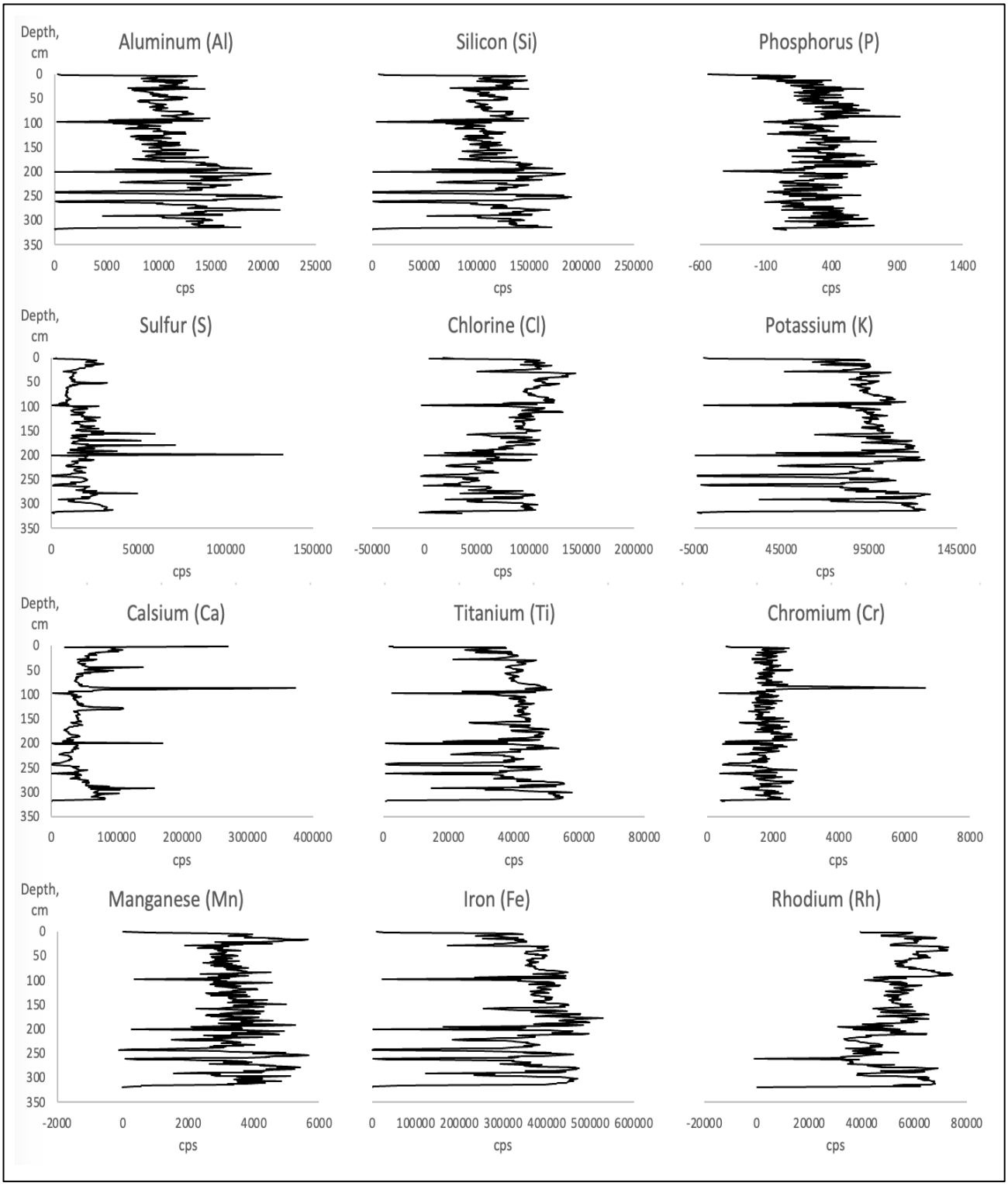

Figure 25. *Core 1070, solid phase elemental counts of Al, Si, P, S, Cl, K, Ca, Ti, Cr, Mn, Fe, and Rh. Used voltage: 10 kv.*

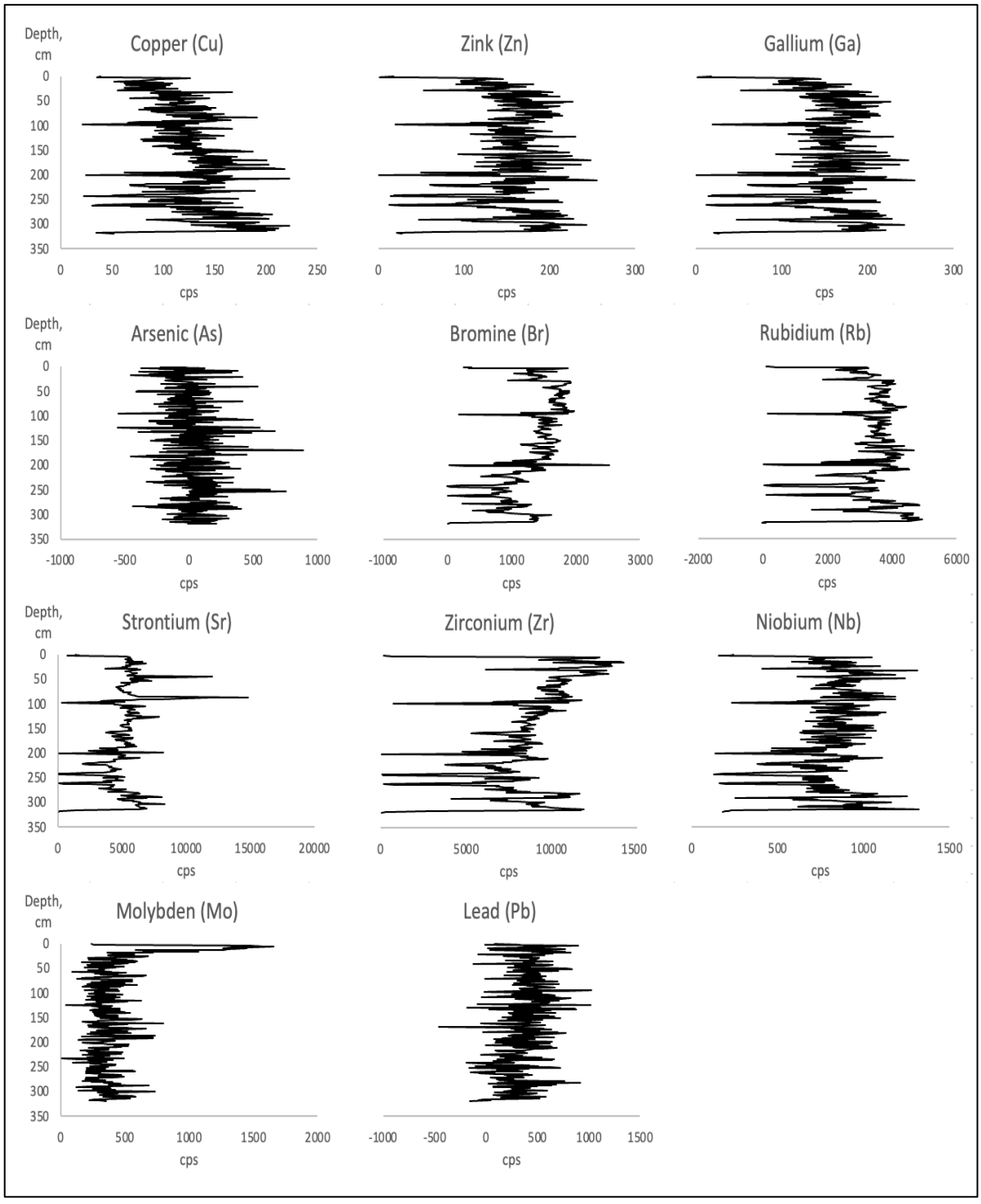

Figure 26. *Core 1070, solid phase elemental counts of Cu, Zn, Ga, As, Br, Rb, Sr, Zr, Nb, Mo, and Pb. Used voltage: 30 kv.*

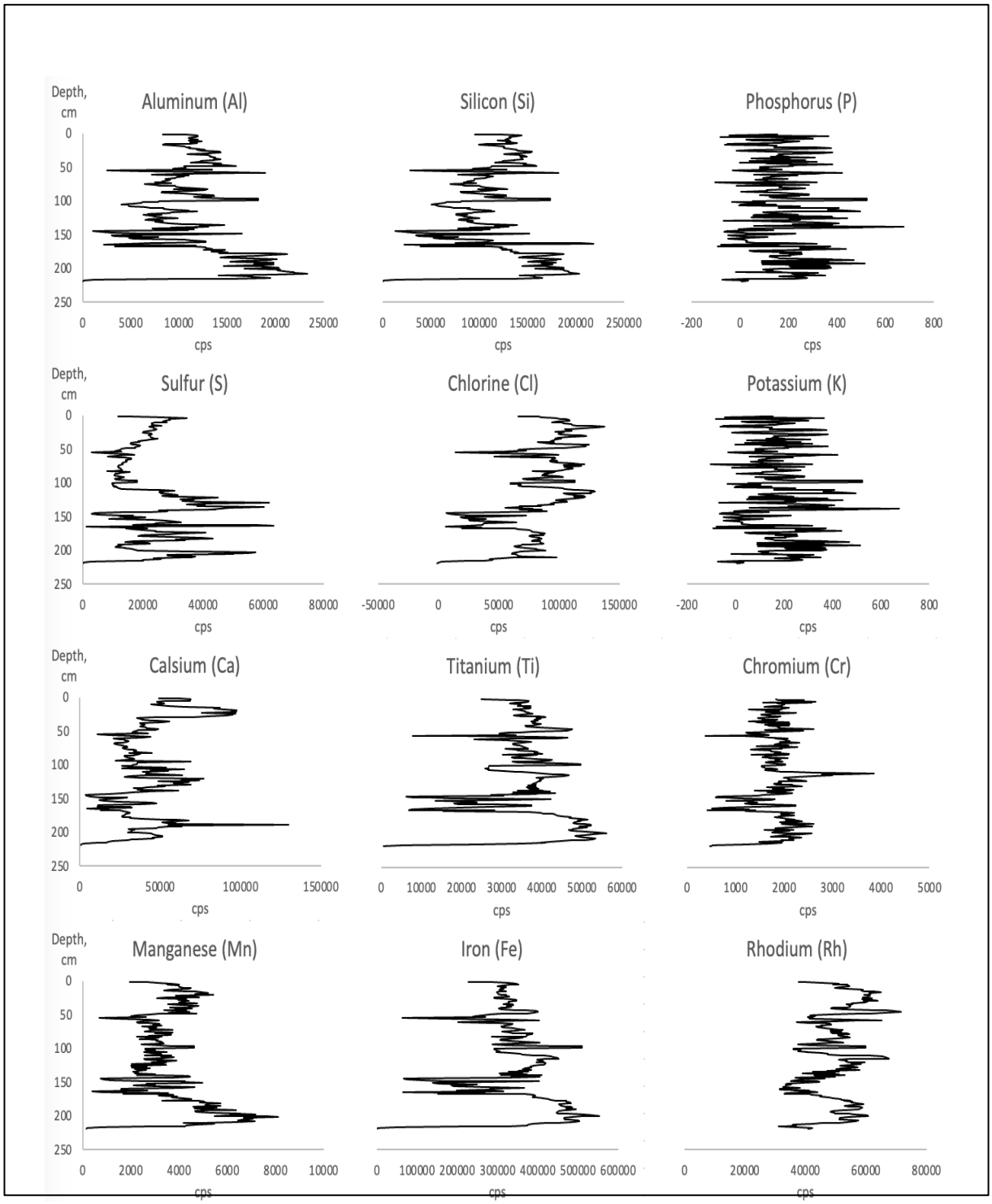

Figure 27. *Core 1069, solid phase elemental counts of Al, Si, P, S, Cl, K, Ca, Ti, Cr, Mn, Fe, and Rh. Used voltage: 10 kv.*

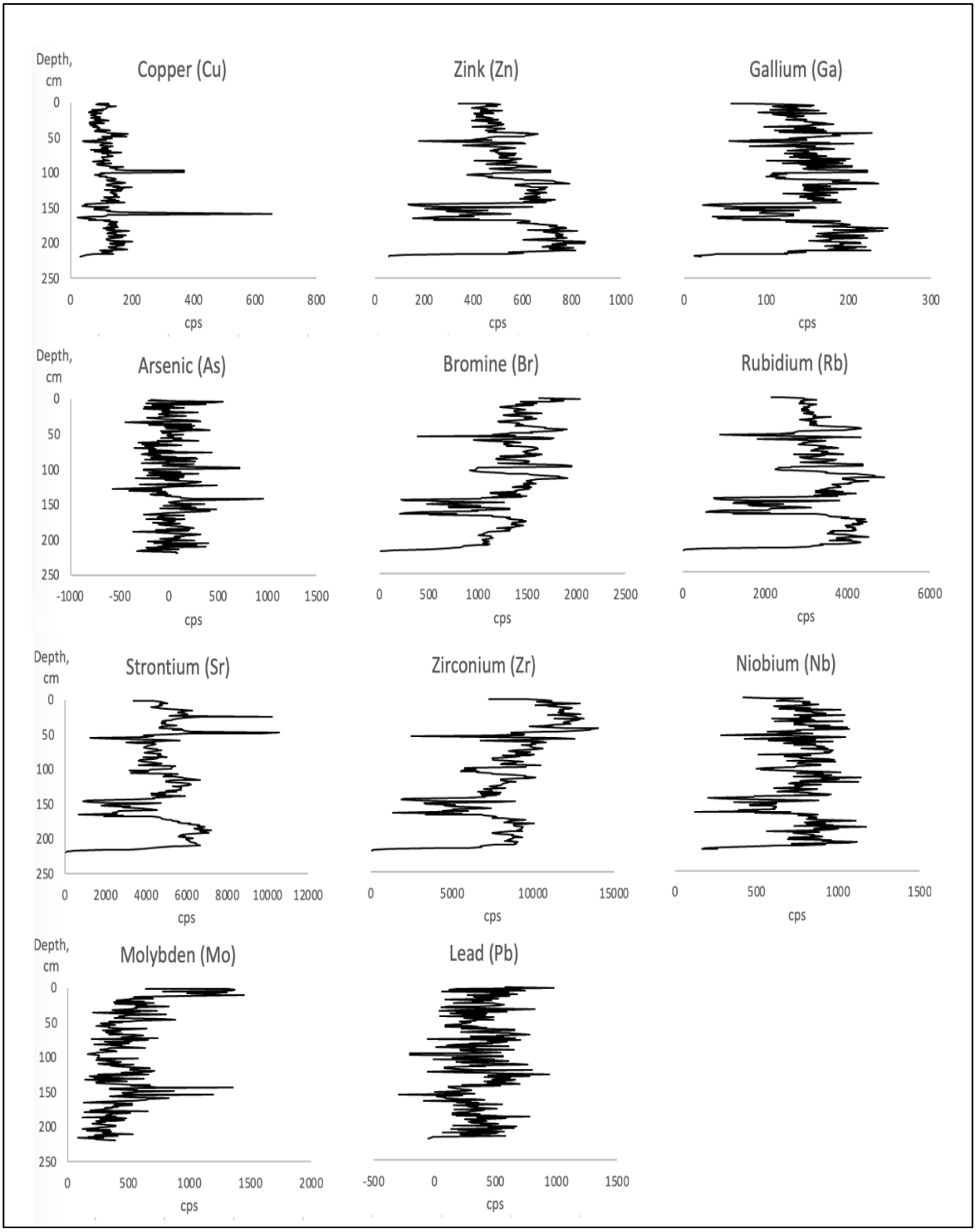

Figure 28. *Core 1069, solid phase elemental counts of Cu, Zn, Ga, As, Br, Rb, Sr, Zr, Nb, Mo, and Pb. Used voltage: 30 kv.*

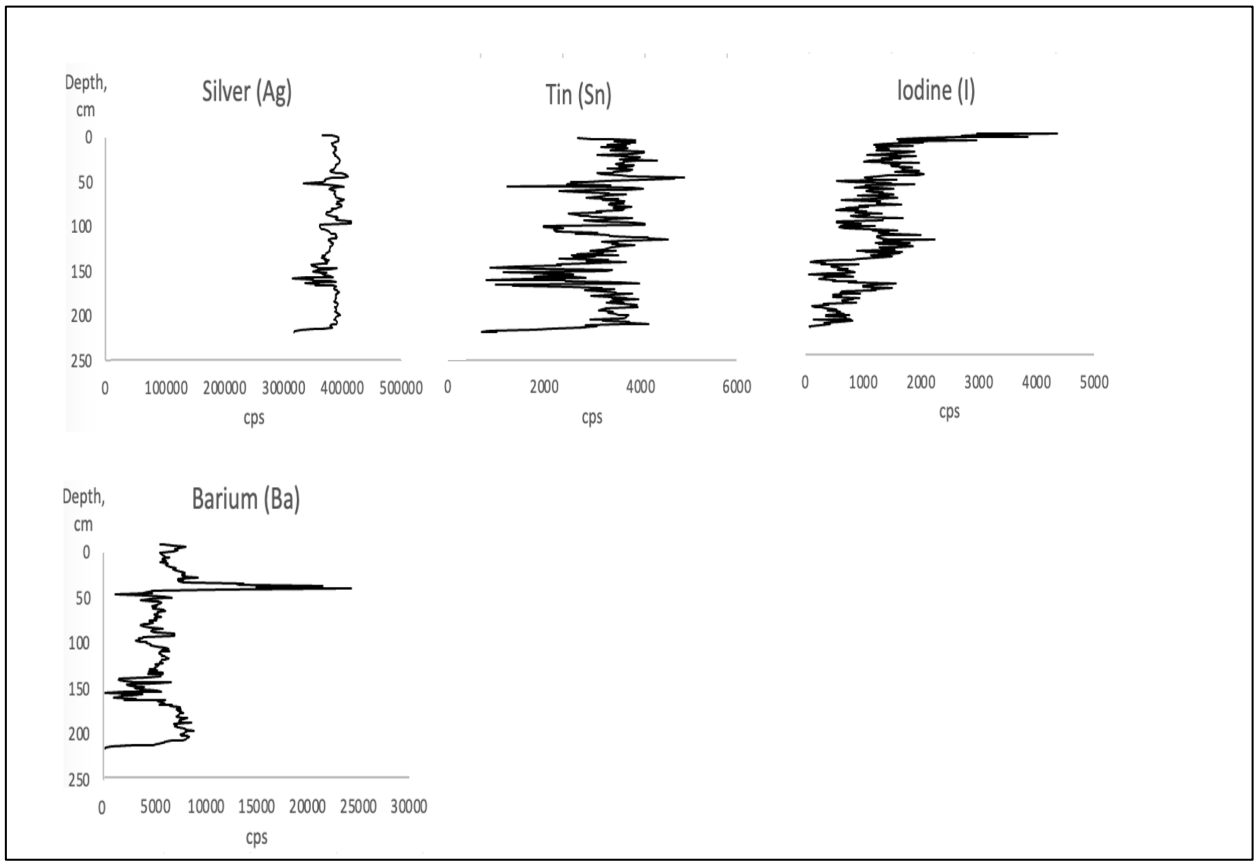

Figure 29. *Core 1069, solid phase element counts of Ag, Sn, I, Ba. Used voltage: 50 kv.*